



Geochemical and Isotopic Characteristics of the Emir Geothermal Waters in Kula Area, Western Anatolia

Ali Gökgöz¹ · Halim Mutlu² · Özgün Demirel³

Received: 12 December 2023 / Accepted: 10 March 2024
© The Author(s) 2024

Abstract

In this study, we investigate chemical and isotopic characteristics of thermal waters of the Emir geothermal field in the Kula region, which hosts the youngest volcanism in Turkey. Studied thermal waters with temperature and electrical conductivity values of 21–63 °C and 3840 to 5210 $\mu\text{S}/\text{cm}$ are of Na–HCO₃ type and have neutral character. $\delta^{18}\text{O}$ and δD of thermal waters are – 9.40 to – 8.41‰ and – 64.16 to – 56.38‰ (VSMOW) and indicate a meteoric source with local recharge. Tritium values of thermal waters in the Emir geothermal field are mostly < 1 TU signifying a deep circulation. Positive $\delta^{13}\text{C}$ values (1.32–4.46‰ VPDB) imply that carbon is derived dominantly from marine limestone and dominantly from endogenic CO₂. $\delta^{18}\text{O}$ and $\delta^{34}\text{S}$ of dissolved sulfate yield that marine limestone is the source of sulfur in thermal waters, which are partly affected by sulfide oxidation and bacterial reduction processes. At discharge temperatures, Emir thermal waters are oversaturated with respect to albite, aragonite, calcite, α -cristobalite, dolomite, gibbsite, illite, K-feldspar, kaolinite, muscovite and quartz but undersaturated for anhydrite and wairakite. The activity diagrams suggest that high Na⁺ and K⁺ concentrations in waters are attributed to dissolution of muscovite, K-feldspar and albite. Chemical and isotopic compositions of the Emir thermal waters are controlled by a combination of processes including water–rock interaction, dissolution/precipitation and ion exchange. Various chemical and isotopic geothermometers applied to the thermal waters yielded reservoir temperatures in the range of 80–125 °C. Paleo-temperatures estimated from $\delta^{18}\text{O}$ values of travertines and thermal waters (isotope fractionation) are consistent with modern discharge temperatures.

Keywords Hydrochemistry · Geothermometry · Paleo-temperature · Emir geothermal waters · Turkey

1 Introduction

Following the closure of Neotethys Ocean in the late Mesozoic, Turkey witnessed an intense post-collisional magmatism that generated plutonic and volcanic rocks spanning a wide of compositions and ages [1]. The collision between

the Arabian and the Anatolian plates in the Miocene resulted in westward movement of Anatolia along two major transform plate boundaries, the North Anatolian Fault Zone (NAFZ) and the East Anatolian Fault Zone (EAFZ) [2, 3] (Fig. 1a). In western Turkey, the compressional regime is transformed to extensional tectonism, which prevailed since at least the Late Miocene. This has led to the development of a number of E–W trending graben systems in the region [2] (Fig. 1b). The western Turkey comprises large volumes of Neogene–Quaternary volcanics with different petrogenetic affinities (Fig. 1b). According to Güleç and Hilton [4], western Anatolia hosts three different volcanic associations, which display some temporal and spatial similarity: Lower–Upper Miocene calc-alkaline, Middle Miocene–Pliocene potassic alkaline and Upper Miocene–Quaternary sodic alkaline lavas. The nature of volcanism shows a transition from dominantly calc-alkaline in the Oligo–Miocene to alkaline in late Miocene–Quaternary times, nearly consistent with the

✉ Ali Gökgöz
agokgoz@pau.edu.tr

Halim Mutlu
halimmutlu@ankara.edu.tr

Özgün Demirel
ozgundemirel1121@gmail.com

¹ Department of Geological Engineering, Pamukkale University, Denizli, Turkey

² Department of Geological Engineering, Ankara University, Ankara, Turkey

³ Graduate School of Natural and Applied Sciences, Pamukkale University, Denizli, Turkey



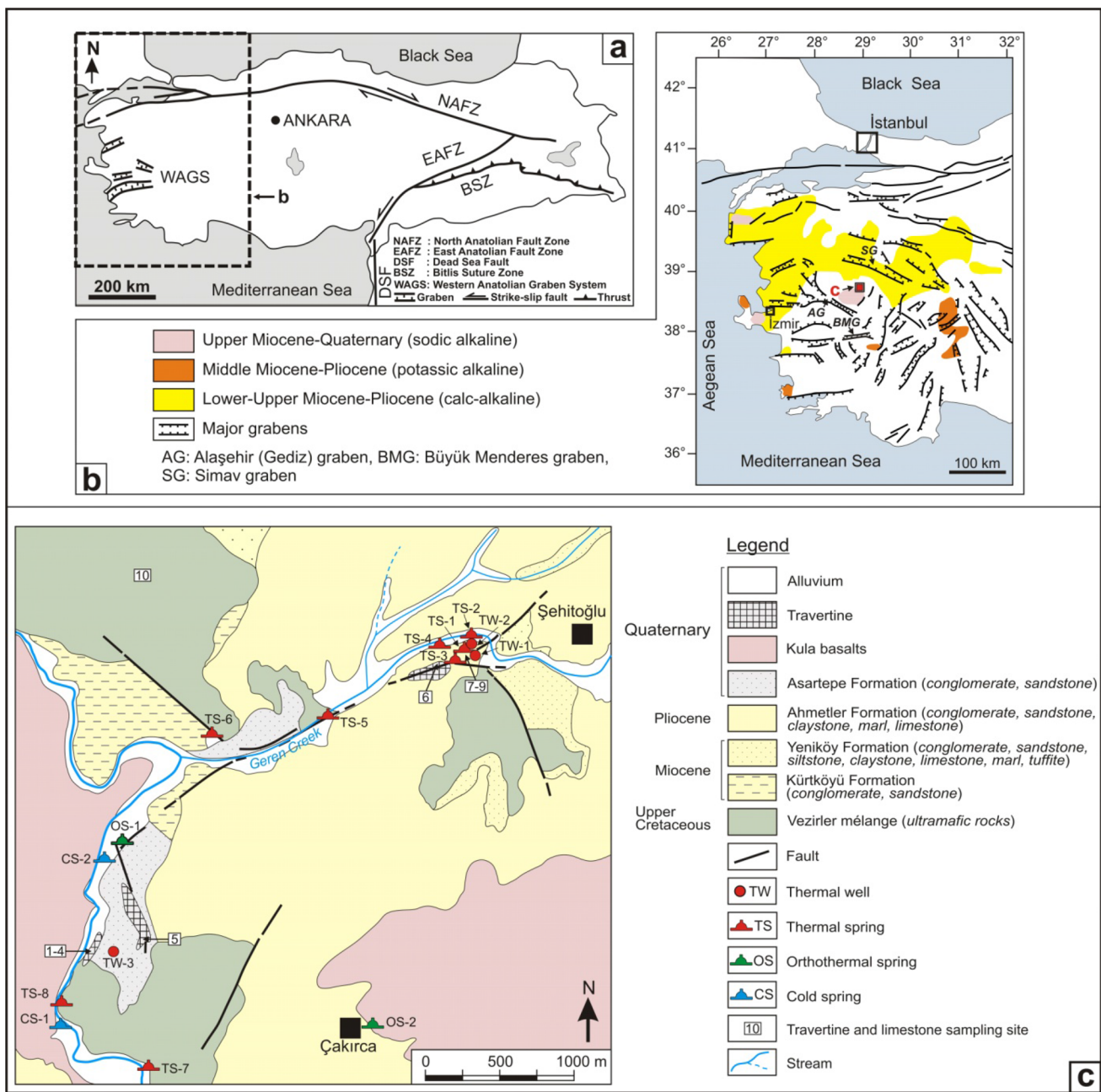


Fig. 1 a Major tectonic structures in Turkey, b Tectonomagmatic map of the western Anatolia showing Miocene–Quaternary volcanics and major graben systems (modified from Mutlu et al. [10]), c Geology map

of the Emir geothermal area with the water sample locations (modified from Akkuş et al. [8])

transition from compressional to extensional tectonics in the region [5, 6].

The tectonomagmatic evolution of Turkey gave rise to development of numerous geothermal fields throughout Anatolia. The highest geothermal energy potential in Turkey is associated with the West Anatolian extensional tectonics, which provides a deep-seated heat source and the occurrence of a series of grabens allowing deep circulation of fluids

[7]. Although the central and eastern Anatolian regions host several sub-active/active volcanoes with historical eruptions, comprising a potential heat source, the relatively moderate geothermal energy potential can be ascribed to the absence of well-developed fault systems [7]. The Kula area between the Simav and Alaşehir grabens in western Turkey contains a low-temperature geothermal system. Thermal waters in the Emir geothermal field (EGF) temperature of 21.1–63.3 °C

Table 1 Chemical compositions of waters from the Emir geothermal field

No	<i>t</i>	EC	pH	Ca ²⁺	Mg ²⁺	Na ⁺	K ⁺	Cl ⁻	SO ₄ ²⁻	HCO ₃ ⁻	NO ₃ ⁻	F ⁻	Br ⁻	Li ⁺	B	SiO ₂	Sr
TW-1	63.3	4920	7.11	90.2	90.9	974.8	90.0	156.7	110.3	3233	0.14	1.77	0.42	1.32	7.74	125.0	3.24
TW-2	56.6	4770	6.95	94.7	97.7	957.2	89.5	163.2	111.3	3233	0.25	1.65	0.41	1.25	7.84	114.3	2.95
TW-3	39.1	5210	6.73	126.3	123.2	1025.4	89.9	205.6	81.2	3477	0.00	1.38	0.50	1.33	9.57	91.6	2.94
TS-1	52.0	4060	6.87	61.5	73.4	806.6	81.6	175.6	103.1	2562	4.33	1.20	0.34	1.02	5.73	100.9	1.96
TS-2	41.1	4050	7.69	35.6	67.6	819.4	77.8	173.8	106.3	2501	8.50	1.20	0.34	1.04	5.78	103.0	1.97
TS-3	55.0	4840	7.01	59.6	86.2	991.7	84.0	159.9	117.2	3172	0.00	1.63	0.39	1.23	7.35	116.3	2.27
TS-4	35.5	3840	6.84	89.8	83.5	717.8	76.1	193.2	102.9	2501	11.27	1.33	0.28	0.85	4.88	103.1	4.20
TS-5	31.4	4370	6.75	109.3	99.5	899.1	68.8	117.6	154.7	3172	0.28	2.03	0.29	0.95	5.44	80.9	2.47
TS-6	21.1	4150	6.56	116.8	121.4	814.1	66.6	115.6	154.1	2806	7.65	1.65	0.29	0.93	5.51	62.7	2.47
TS-7	38.2	4660	6.78	108.9	123.6	819.0	81.2	171.2	102.3	3111	2.11	1.23	0.44	1.20	8.97	88.7	2.87
TS-8	36.1	4960	6.72	100.5	116.5	1022.6	86.4	209.9	105.0	3294	1.21	1.51	0.49	1.27	9.22	84.2	2.82
OS-1	15.5	3510	6.31	301.9	138.5	460.4	52.6	160.7	30.0	2456	8.19	0.36	0.28	0.61	2.82	53.5	1.66
OS-2	18.4	710	7.72	49.8	29.7	51.7	18.3	20.5	11.2	323	92.69	0.18	0.07	0.01	0.05	39.5	0.75
CS-1	11.8	1130	7.79	103.4	40.9	89.0	42.5	203.3	45.0	427	32.38	0.18	0.07	0.01	0.10	25.1	0.43
CS-2	12.8	1550	6.71	124.1	52.7	145.2	49.7	256.3	52.2	680	33.70	0.00	0.08	0.02	0.09	14.4	0.30
RW		39	8.11	10.0	0.4	0.4	0.42	0.1	0.8	31	0.96	0.01	n.d	n.d	n.a	n.a	n.a

t Measured sampling temperature (°C), *EC* electrical conductivity (μS/cm), concentrations are in mg/L. *TW* thermal well, *TS* thermal spring, *OS* orthothermal spring, *CS* cold spring, *RW* rain water. *n.d.* not detected. *n.a.* not analyzed. Sample numbers correspond to locality numbers given in Fig. 1c

are manifested along a NE-SW trending normal fault within the Geren Creek (Fig. 1c). Geothermal wells have depths of 33 to 163 m with artesian discharge of 40–100 L/s [8]. Total discharge of springs is reported 12.2 L/s [8]. The EGF thermal waters are utilized for balneology and a mineral spring (Kula mineral water, OS-1 in Table 1) in the area is bottled for commercial use. In addition, young lavas (dated at 2.5 ka BP) and spectacular volcanic structures (e.g., human footprints in a volcanic ash layer dated 4.7 ka BP) in Kula have been included in the Geopark list by UNESCO [9].

In this study, we investigate the geochemical and isotopic characteristics, and processes affecting the chemistry and mineral equilibrium of the EGF thermal waters. Major ion chemistry and stable isotope compositions (oxygen, hydrogen, carbon and sulfur) of the waters are used to determine the source of the thermal fluids and predict the reservoir temperatures. Equilibrium states of the EGF thermal waters were examined using the Na–K–Mg triangular diagram, activity diagrams constructed by the ratios of major cations and saturation diagrams, which provided a complementary data for the estimation of reservoir temperature.

2 Geological and Hydrogeological Setting

The metamorphites of the Menderes Massif (not shown in the geological map in Fig. 1c) represented by the Paleozoic Eşme Formation and Musadağı marbles, which comprise the basement lithologies in the study area. The Eşme Formation is overlain by cover schists of the Menderes Massif and alternated with thin marble bands [11].

The Vezirler Mélange consisting of ultramafic rocks, radiolarite, cherty limestone, mudstone, mafic volcanites and marble tectonically overlies the Massif [11]. The mélange units are unconformably covered by two separate Miocene formations. The Kürköyü formation consists of mudstone, sandstone and conglomerate derived from mélange and metamorphites [11]. Above is the Yeniköy formation that is composed of conglomerate, sandstone, siltstone, claystone, clayey-sandy limestone, marl and tuffite alternation, and gypsum lenses deposited in a fluvial environment [11]. The overlying Pliocene Ahmetler formation is made up of horizontally bedded conglomerate-sandstone, claystone, marl, tuffite and limestone. The Quaternary Asartepe formation is composed of conglomerate-sandstone alternation.

The Kula volcanic field located SW of the study area comprises numerous monogenetic eruption centers including cinder cones, tumulus and maars [12, 13]. It is an alkali basalt province in an area of active rifting. The volcanic products are classified as basanite and phonotephrite [6]. The volcanism in Kula is reported to span from Plio-Quaternary to Holocene and is classified into three different stages. The Burgaz stage dating from 1.1 to 1.37 Ma occurs as plateau basalts on the hills [14]. The second stage, so-called Elekçitepe, is dated at 0.17–0.24 Ma [15] and represented by base surge deposits. The Divlittepe is the youngest phase of volcanism (2.5–13.1 ka BP [15, 16]) and comprises fresh lava flows of tens of kilometers extending along the valleys. The Kula lavas are suggested to be derived from asthenospheric and lithospheric sources [6, 17, 18]. Travertines are precipitating from thermal waters that issue through the faults and extensional fissures.



Roll-back subduction beneath Hellenic Arc resulted in back arc extension in the Aegean and formation of Aegean graben system, E-W oriented graben system and associated high enthalpy geothermal fields [19–23]. The thinning of the lithosphere has increased the geothermal energy potential of the region and recent seismic activity in the region caused several devastating earthquakes [19]. The young tectonomagmatic activity resulted in a high geothermal gradient. Based on silica temperature estimations, heat flow in the study area is found 123 mW/m^2 [24, 25]. However, in a more recent study by Bilim et al. [26], the heat flow in Kula is reported 240 mW/m^2 (almost twice the former) and depth of the shallowest Curie point in the same area is found 6.21 km. All these findings imply that Neotectonic activity is the possible heat source in the EGF.

The study area is located in the transition zone between the Mediterranean climate, which is generally hot and dry in summers and warm and rainy in winters, and the continental Central Anatolian climate, which is hot and dry in summers and rainy and cold in winters. According to systematic measurements carried out at the Kula meteorological station, the average annual air temperature in the study area is $14.77 \text{ }^\circ\text{C}$ and the average annual total precipitation is 466 mm.

The Eşme Formation metamorphites are impermeable or slightly permeable. The overlying Musadağı dolomitic marbles are quite fractured and therefore have high permeability. The Vezirler mélange with a fractured and faulted structure has high secondary porosity and permeability. The Neogene sedimentary units are permeable and form the local aquifers. The Quaternary Asartepe formation and alluvium have aquifer characteristics. The Burgaz stage of Kula volcanics, from which spring OS-2 emits, is represented by a high secondary permeability.

Marble, quartzite, quartz schist, dolomitic marble of the Menderes Massif and limestones and intensely fractured serpentines of the Vezirler mélange comprise thermal reservoir in the EGF. Impermeable or less permeable lithologies (e.g., claystone, siltstone, marl) of Neogene units are the possible cap rocks.

3 Materials and Methods

A total of 16 waters were sampled in the EGF from three thermal wells, eight thermal springs, two orthothermal springs, two cold springs and one rainwater. Temperature, pH and electrical conductivity (EC) values of water samples were measured onsite by using Hach Lange HQ40D portable dual input multi-parameter meter. Before the each measurement, the device was calibrated with standard solutions. Waters for anion analysis were filtered ($0.45 \text{ }\mu\text{m}$) and collected into double-plugged 250-mL high-density polyethylene (HDPE) bottles. Sampling for cation and trace element analyses was

done separately into 100-mL HDPE bottles and then ultrapure HNO_3 added to prevent precipitation. The batch taken for SiO_2 analysis was diluted with ultrapure water.

Samples for oxygen–hydrogen isotope and tritium analyses were collected by filtering into 50-mL and 500-mL double-plugged HDPE bottles. For $\delta^{13}\text{C}$ (dissolved inorganic carbon) analysis, waters were sampled by filtering into brown glass containers and stored in the cold chain ($< +4 \text{ }^\circ\text{C}$). Waters for $\delta^{34}\text{S}$ and $\delta^{18}\text{O}$ (sulfate) analyses were filtered and ultrapure HCl was added to lower pH to 4–5. Then, by adding 150 mg $\text{BaCl}_2 \cdot 2\text{H}_2\text{O}$, BaSO_4 was precipitated. For $\delta^{18}\text{O}$ and $\delta^{13}\text{C}$ analyses and XRD determinations, limestone and travertine samples were powdered.

Anion (Cl^- , SO_4^{2-} , HCO_3^- , F^- , Br^- and NO_3^-), cation (Na^+ , K^+ , Ca^{2+} , Mg^{2+} and Li^+) and tritium analyses of waters were conducted at the Water Chemistry and Environmental Tritium Laboratory of the Hacettepe University. Concentrations of anion and cation were determined using a high performance ion chromatography device (Chromleon Dionex). An ICS 1000 and LC 25 were used for analyzing anions and cations, respectively. HCO_3^- was measured by titration method using methyl orange as indicator solution and 0.01 N H_2SO_4 as titrant solution. Tritium analysis was carried out by the liquid scintillation (Perkin Elmer Quantulus) counting method. Trace element (B, Sr and other 68 elements) contents were measured at Bureau Veritas Mineral Laboratories by ICP-MS method. Concentrations of most elements were less than the laboratory's method detection limits (MDL) (< 0.01 to < 10 ppb). SiO_2 was analyzed with spectrophotometric technique (HACH DR/4000) at the Geochemistry Laboratory of the Pamukkale University.

$\delta^{18}\text{O}$ and δD of the waters were analyzed at the Technical Research and Quality Control Department of the State Hydraulic Works (DSI) by using laser spectrometer method (WS-CRDS, Wavelength-Scanned Cavity Ring-Down Spectroscopy). Analytical precisions are 0.05/0.15‰ for $\delta^{18}\text{O}/\delta^2\text{H}$ reported relative to Vienna Standard Mean Ocean Water (VSMOW). The $\delta^{34}\text{S}$ (VCDT) and $\delta^{18}\text{O}$ (VSMOW) of sulfate and $\delta^{13}\text{C}$ (VPDB) of dissolved inorganic carbon (DIC) were measured at the Environmental Isotope Laboratory of the University of Waterloo, Canada. The analysis of $\delta^{34}\text{S}$ was carried out through thermal conversion of sample material to gas through an 4010 Elemental Analyzer (Costech Instruments, Italy) coupled to a isoprime precISION (Elementar Americas, USA) continuous flow isotope ratio mass spectrometer (CFIRMS). The analysis of BaSO_4 for $\delta^{18}\text{O}$ measurement was conducted through high-temperature ($1450 \text{ }^\circ\text{C}$) pyrolysis combustion conversion of sample material to CO gas. This was accomplished using an Elementar Vario Pyro Cube elemental analyzer coupled to an Isoprime (GV Instruments) CFIRMS. The analytical precision for both analyses is 0.3‰ (2σ). For $\delta^{13}\text{C}$ (DIC) analysis,

0.2 mg carbonate is injected into a helium flushed 12 mL Lab-coExetainer vial. A small volume of 85% phosphoric acid (H_3PO_4) was used for the complete reaction of the inorganic carbon to convert to CO_2 in the headspace. The vials were then placed in a CTC PAL autosampler and analyzed with a Thermo Scientific Gas-bench coupled to a Thermo Scientific Delta V Plus isotope ratio mass spectrometer. Results of analyses were reported at 2-sigma error range with precision of 0.2‰. $\delta^{18}\text{O}$ and $\delta^{13}\text{C}$ of limestone and travertine samples were carried out at the Central Laboratory of the Middle East Technical University using the Gas-Bench-Continuous Flow Isotope Ratio Mass Spectrometry (Thermo Finnigan Delta-Plus XP). Results are given as ‰VPDB (Vienna Pee Dee Belemnite). The analytical precision does not exceed 0.2‰.

XRD analysis of travertine samples was conducted with Shimadzu XRD-6000 model X-ray diffractometer (Ni-filtered, $\text{CuK}\alpha$ radiation) at the Technology Application Research Center of the Afyon Kocatepe University.

4 Results and Discussion

4.1 Water Chemistry and Sources of Solutes

On-site measurement and sampling of thermal and cold waters in the EGF were carried out during field studies in October 2018, and rainwater was sampled in November 2018. Analysis results are given in Table 1. Charge-balance of waters falling the range between 2.43 and -4.96% is within the acceptable limit of $\pm 5\%$. The results of analyses are consistent with previous studies that reported water chemistry data for some of samples in the EGF [27–29].

In the EGF, the temperatures of waters vary between 11.8 and 63.3 °C (Table 1). There are several suggestions regarding the classification of waters with respect to their temperature [30–32] and in previous studies different classifications were used [33, 34]. According to the Schoeller [30] classification that is adopted in this study (as T and T_a are the spring and average annual air temperatures, respectively), if $T > T_a + 4$ °C, the spring is classified as thermal water, and if $T_a < T < T_a + 4$ °C, spring is regarded as an orthothermal type. Accordingly, among the sampled waters, CS-1 and CS-2 springs are cold waters ($T < 14.8$ °C), OS-1 and OS-2 springs are orthothermal waters ($14.8 < T < 18.8$ °C), and other samples are considered as thermal waters ($T > 18.8$ °C).

Electrical conductivity values are between 1130–1550 $\mu\text{S}/\text{cm}$ for cold waters, 710–3510 $\mu\text{S}/\text{cm}$ for orthothermal waters and vary from 3840 to 5210 $\mu\text{S}/\text{cm}$ for the thermal waters. The pH ranges from 6.71 to 7.79 for the cold waters and 6.31 to 7.69 for the thermal and orthothermal waters (Table 1).

There are several factors that modify the chemical composition of groundwater, which include the type of lithology

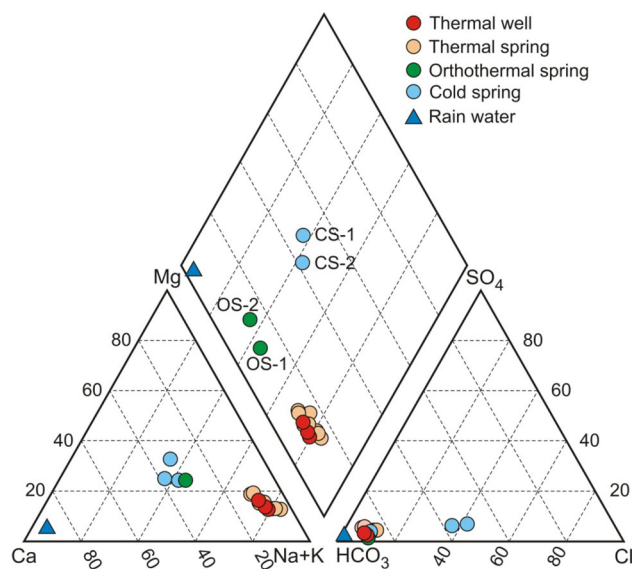
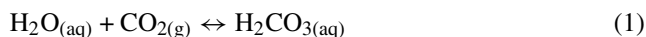


Fig. 2 Piper diagram of the waters

in the geothermal system, temperature, water–rock interaction, boiling, conductive cooling, dissolution/precipitation and mixing with cold groundwater. These processes also define the hydrochemical type of thermal waters. Rainwater falling on the recharge area of the EGF dissolves the atmospheric and soil CO_2 and gains a slightly acidic character:



Meteoric water that percolates underground through pores, cracks and fractures chemically reacts with the minerals and dissolves them and then becomes enriched with various elements depending on the rock composition. The order of cation (in meq/L) is $\text{Na}^+ > \text{Mg}^{2+} > \text{Ca}^{2+} > \text{K}^+$ for the EGF thermal waters, $\text{Ca}^{2+} > \text{Na}^+ > \text{Mg}^{2+} > \text{K}^+$ for CS-1 and CS-2 springs, $\text{Na}^+ > \text{Ca}^{2+} > \text{Mg}^{2+} > \text{K}^+$ for OS-1 spring, $\text{Ca}^{2+} > \text{Mg}^{2+} > \text{Na}^+ > \text{K}^+$ for OS-2 spring. The order of anion in all waters, except for sample OS-2, is $\text{HCO}_3^- > \text{Cl}^- > \text{SO}_4^{2-}$. Due to the high nitrate concentration in the OS-2 orthothermal spring, the anion order is $\text{HCO}_3^- > \text{NO}_3^- > \text{Cl}^- > \text{SO}_4^{2-}$. Ca^{2+} and HCO_3^- are dominant in rainwater, while other ions have negligibly low concentrations.

In the Piper diagram, the EGF thermal waters plot within the Na- HCO_3 field (Fig. 2). CS-1 and CS-2 cold waters have relatively high chloride contents. These springs with similar chemical composition are of Ca-Na-Mg- HCO_3 -Cl type waters. OS-1 spring is Na-Ca-Mg- HCO_3 type while OS-2 derived from the basalt aquifer is Ca-Mg-Na- HCO_3 type water. Schoeller diagram shows that Ca^{2+} , Mg^{2+} , K^+ , Cl^- , SO_4^{2-} and SiO_2 contents of thermal waters are similar and anion concentrations do not significantly change but there appears to be a relative difference in the Ca^{2+} and Mg^{2+} contents (Fig. 3). Although Na^+ and SO_4^{2-} concentrations of

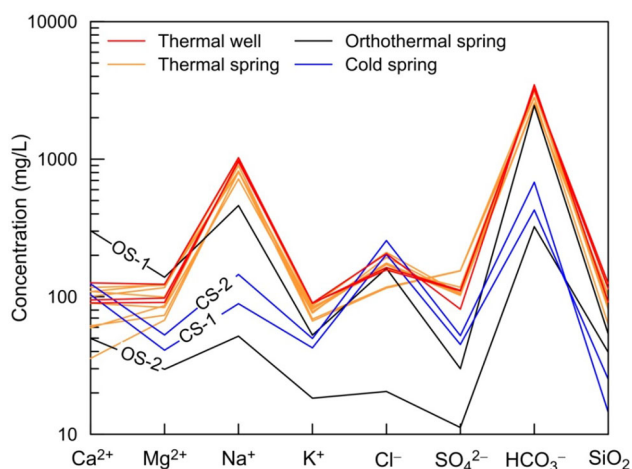
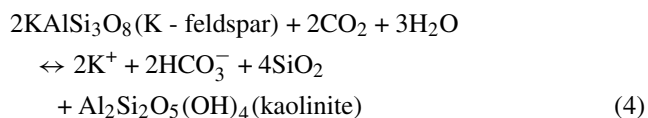
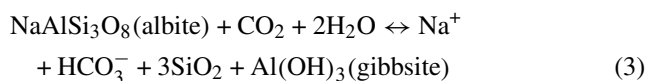
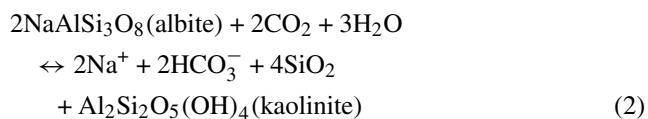


Fig. 3 Schoeller diagram for the waters in the EGF

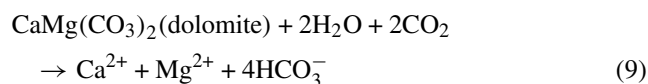
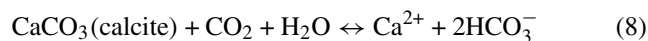
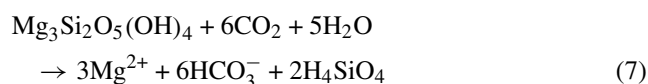
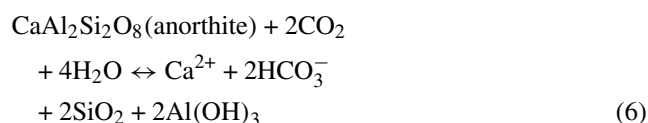
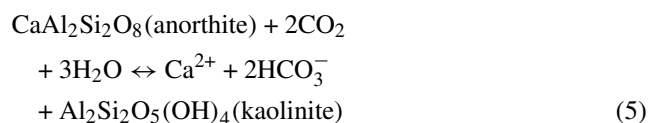
OS-1 are lower than thermal waters, the amount of Ca^{2+} is almost three times higher than most thermal waters.

Na^+ and K^+ concentrations of the EGF thermal waters are 717.8–1025.4 mg/L (average 895 mg/L) and 66.6–90.0 mg/L (average 81 mg/L), respectively. There is a strong positive relationship between $\text{Na}^+ + \text{K}^+$ and HCO_3^- contents of water ($R^2 = 0.98$) (Fig. 4a). In the $\text{Na}^+ + \text{K}^+$ vs. HCO_3^- diagram, all the samples plot very close to but at the left part of 1:1 line, indicating that silicate dissolution exerts a great control on the chemical composition of thermal waters. The same graphic also implies an additional source of HCO_3^- . CO_2 is derived from multiple reservoirs including marine limestone, atmosphere and soil. The main source of Na^+ and K^+ in thermal waters is the dissolution of silicate minerals from the Menderes Massif metamorphics, Vezirler mélange and volcanic units. The dissolution of feldspars to form clay minerals is expressed by the following reactions (Eqs. 2–4):



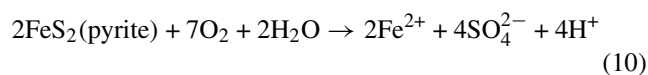
Thermal waters have similar Ca^{2+} and Mg^{2+} concentrations ($\text{Ca}^{2+} = 35.6\text{--}126.3$ mg/L, average 90.3; $\text{Mg}^{2+} = 67.6\text{--}123.6$ mg/L, average 98.5 mg/L). However, HCO_3^- contents are quite high (2501–3477 mg/L, average 3006 mg/L). Ca^{2+} , Mg^{2+} and HCO_3^- must have

been released by dissolution of Ca-plagioclase, marbles, dolomitic marbles in the Menderes massif, serpentinite, limestones/recrystallized limestones in the Vezirler mélange and Pliocene lacustrine limestones (Eqs. 5–9):



There is a weak correlation between $\text{Ca}^{2+} + \text{Mg}^{2+}$ and HCO_3^- contents of the EGF thermal waters ($R^2 = 0.36$) (Fig. 4b). The relatively low Ca^{2+} and Mg^{2+} concentrations are attributed to carbonate (calcite and aragonite) precipitation in association with loss of CO_2 during the rise of thermal waters to the surface. This is supported by scaling in geothermal drilling pipes and widespread travertine deposits at the surface. Cation exchange between water and rock is another reason for the low Ca^{2+} and Mg^{2+} contents. In Fig. 4b, cold and OS-2 waters plot on the 1:1 line. High $\text{Ca}^{2+} + \text{Mg}^{2+}$ contents of OS-1 spring are explained by dissolution of carbonate rocks at relatively shallow depths.

The absence of evaporite deposits (except for local gypsum lenses within the Yeniköy formation) around the Kula area necessitates an alternative source for the sulfur in the EGF waters (Fig. 4c). In previous studies, sedimentary carbonates are reported to host significant amounts of sulfate and their recrystallization might be the source of sulfur [35, 36]. This mechanism, so-called structural substitution of sulfate (carbonate-associated sulfate, CAS) into carbonates, could explain the existence of sulfur in the EGF samples. The dissolution of pyrite in the reservoir rocks can be considered as an alternative source of sulfate in waters. By the oxidation of pyrite within the Vezirler mélange (Eq. 10), Fe^{2+} and SO_4^{2-} are released into the water.



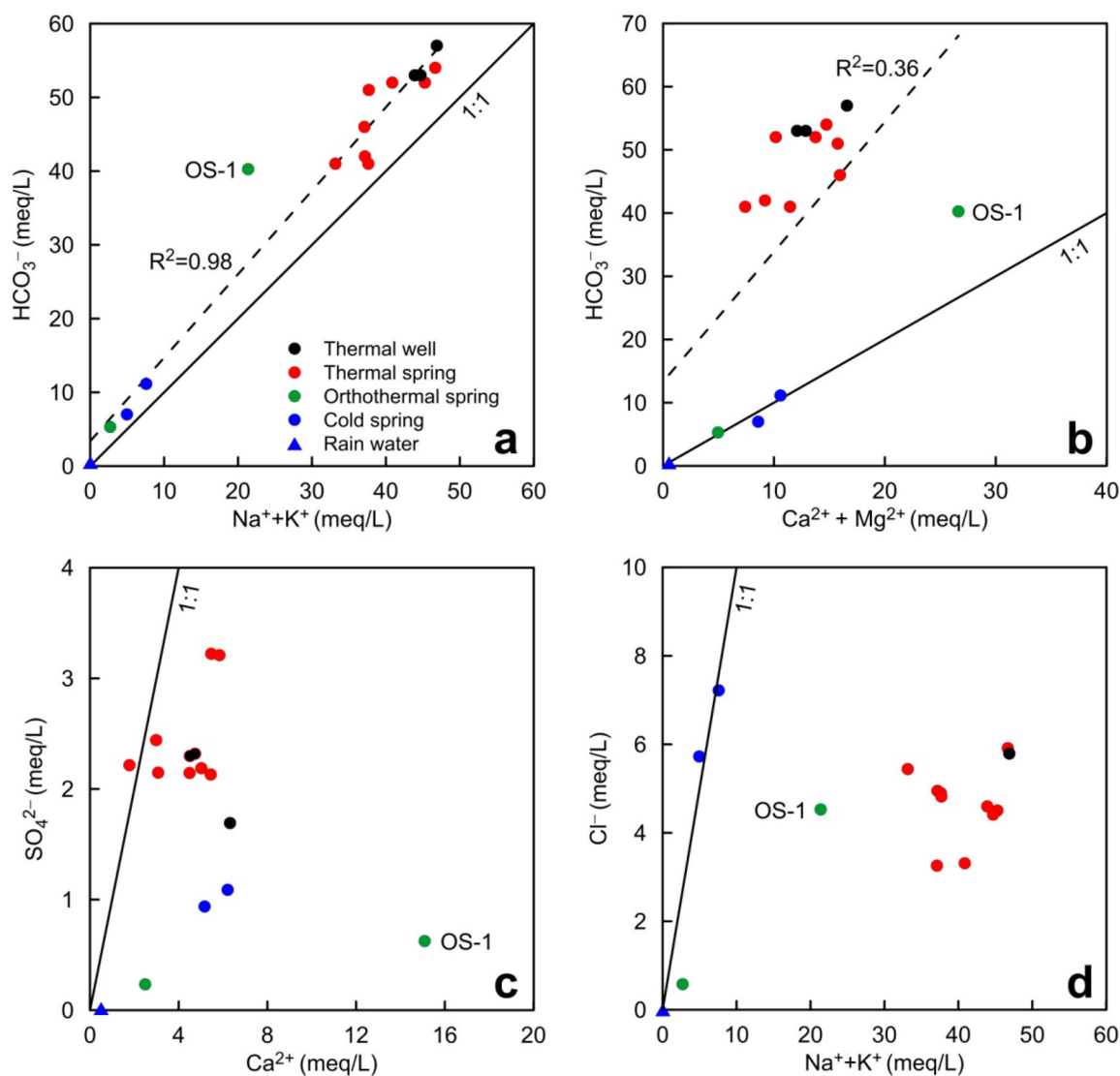


Fig. 4 Binary ion diagrams showing the origin of dissolved solids in the EGF waters

Water that gained an acidic character is buffered by the dissolution of silicates and carbonates that brings the pH to weakly acidic or neutral values. Sulfate was later reduced to form hydrogen sulfide, which was manifested by a strong rotten egg odor emanating from the EGF thermal waters. Gypsum lenses of the Yeniköy formation might also provide a limited contribution SO_4^{2-} , together with Ca^{2+} ions.

Na^+ and Cl^- in thermal waters are weakly correlated and the molar Na^+/Cl^- ratios are greater than 5 (Fig. 4d). Sodium excess in waters is due to silicate alteration and cation exchange process. The $(SO_4^{2-}+HCO_3^- - Ca^{2+}-Mg^{2+})$ vs $(Cl^- - Na^+ - K^+)$ diagram is very helpful to show the effect of ion exchange on the groundwater chemistry [37]. In Fig. 5, all thermal waters plot on the ion exchange line indicating the cation exchange process exerts a great control on the chemical composition of the samples. Base-exchange index

($BEI = (Cl^- - (Na^+ + K^+))/Cl^-$, in meq/L [38]) of thermal waters varies from -5.1 to -11.3 . In waters issuing from the metamorphic and sedimentary rocks, BEI values are generally negative due to the fact that the amount of alkali ions released into water is much more than Cl^- content that results from the silicate dissolution [39]. The negative BEI value indicates exchange of Ca^{2+} and Mg^{2+} in waters with Na and K in minerals. Na^+/Ca^{2+} molar ratio of waters is generally 4–9; however, this ratio in samples TS-1, TS-2 and TS-3 is up to 11–20 due to carbonate precipitation and the extent of cation exchange reactions.

According to Huang et al. [40], fluid inclusions in natural serpentinites contain up to 50 wt.% chlorine. Experimental data show that some water-soluble elements (e.g., Cl and B) are accumulated as salt complexes on the crystal

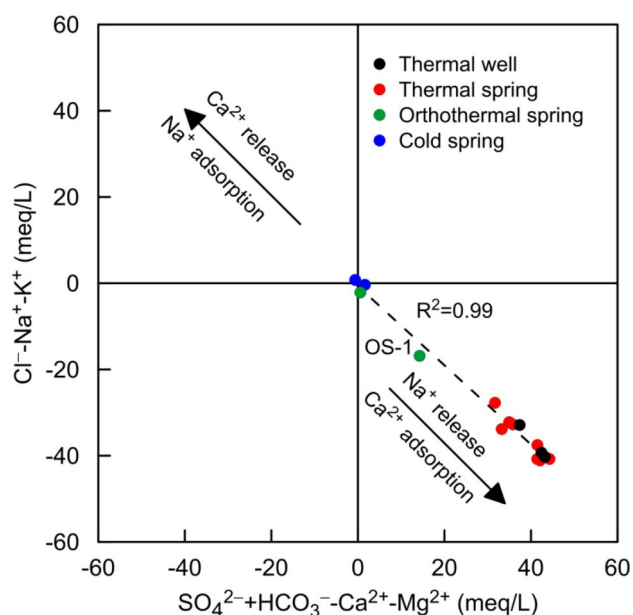


Fig. 5 Bivariate plot of $(\text{SO}_4^{2-} + \text{HCO}_3^- - \text{Ca}^{2+} - \text{Mg}^{2+})$ vs. $(\text{Cl}^- - \text{Na}^+ - \text{K}^+)$

surface or along the micro cracks [41]. Consequently, considerable amounts of the minor components such as Cl, B and F are released into solution from the rocks along with SiO_2 and alkalis [42]. Chloride may replace hydroxyl ions within amphibole, mica and clay minerals. In the lithological log of TW-2 well, thick clay zones were observed within the serpentinites [8]. The fine-grained lithologies of the Neogene units, mudstones and argillization zones within the Menderes Massif metamorphics and the Vezirler mélangé are the likely sources of chloride in thermal waters.

Electrical conductivity and major ion contents of CS-1 and CS-2 waters are higher than the expected values for cold springs (Table 1). Particularly high Cl^- concentrations of these samples (up to 256 mg/L) might be explained by dissolution of serpentine minerals. Chlorine can be hosted in a structurally bound site, substituting for the hydroxyl group in serpentine minerals [43], or in a water-soluble site [44]. Studies on chlorine distribution in serpentinites showed that serpentine minerals contain up to 0.8 wt% Cl^- [44–46]. According to Sharp and Barnes [47] and Huang et al. [48], serpentine minerals lose some amount of chlorine during their equilibration in dilute water at ambient temperature.

The CS-1 and CS-2 springs are issued from the alluvium. However, due to its low extent and thickness around the locations of springs C-1 and C-2, alluvium is not considered an aquifer. The C-1 spring discharges from the Vezirler mélangé that hosts limestone blocks up to 700×400 m in size. The chemical composition of the spring reflects dissolution of serpentine and limestone. Since the spring water

does not discharge from an aquifer consisting solely of ultramafic rocks, it is not Mg- HCO_3 type. CS-2 spring is emitted along the fault that also provides the outlet of the OS-1 spring and discharges groundwater through the conglomerates with ultramafic pebbles. It is suggested that serpentine minerals within the Vezirler Mélangé and Kürtköyü formation are likely to be source of elevated chlorine concentrations in cold springs. In addition, since these two springs are manifested within the streambeds they are polluted by mixing with stream water ($\text{NO}_3^- = 33$ mg/L). OS-2 spring is issued in the residential area and is also possibly contaminated by domestic pollutants ($\text{NO}_3^- = 92.7$ mg/L).

F^- , Li^+ , B, Sr and SiO_2 contents of the EGF waters increase with increase in temperature (Fig. 6). Particularly, there is a strong positive correlation between temperature and SiO_2 ($R^2 = 0.88$) (Fig. 6a). Na^+ and K^+ concentrations in waters also increase with temperature. B and Sr concentrations of the EGF thermal waters with ranges of 4.8–9.2 mg/L and 1.9–4.2 mg/L (Fig. 6b) are higher than most thermal waters in the western Anatolia. In geothermal fields within the Menderes massif, except for the seawater mixing, water–rock interaction is likely to be the sole process for the source of boron in waters [7]. Tokçaer [49] stated that boron participates into the crystal structure of several minerals (e.g., muscovite, plagioclase biotite, K-feldspar, quartz and garnet) by ionic replacement. As a result of intensive water–rock interaction, it is released into water with increase in temperature and prolonged reaction time. According to Vengosh et al. [50], boron in the geothermal waters of the Menderes massif is derived from water–rock interaction rather than deep mantle input as $\text{B}(\text{OH})_3$. Boron is particularly accumulated in the quartz veins, tourmaline gneiss, illite–chlorite–feldspar zone and quartz–chlorite schist zone. They also emphasize that boron and lithium concentrations in the thermal waters vary with depth and lithology. Similarly, $^{87}\text{Sr}/^{86}\text{Sr}$ ratios of thermal waters in western Anatolia show that Sr is derived from a highly radiogenic source (e.g., schists and quartzites) in the reservoir [50].

F^- and Li^+ concentrations of the EGF thermal waters are 1.20–2.03 and 0.85–1.33 mg/L, respectively. Fluorite (CaF_2) is the major mineral of fluorine. The gneiss within the Menderes massif contains fluorite. Fluorine is also hosted in amphibole, mica and apatite, which are common minerals of the Eşme formation [12]. In crystal structure of these minerals, fluorine exists as F^- and can replace hydroxyl due to similar radius and charge [51]. Clay minerals with high anion exchange capacity can capture fluorine under near-neutral pH conditions [52]. The strong correlation of lithium with fluorine strongly suggests their common a crystallochemical association in micas of the Menderes metamorphic rocks (Fig. 6c) [53].

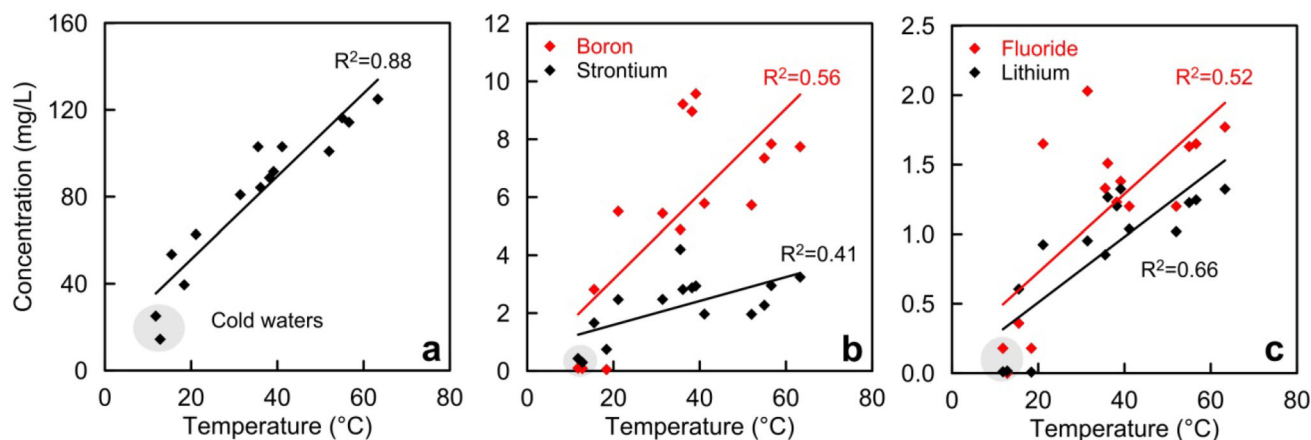


Fig. 6 Variations in element concentrations with temperature, **a** silica, **b** boron and strontium and **c** fluoride and lithium

4.2 Mineral Saturation and Mineral-Fluid Equilibria

Mineral saturation calculations are essential since they provide information on the type of scaling that may arise during the production, operation and transportation of thermal waters. Tackling the scaling in boreholes and pipelines brings an additional cost to operating expenses. For this reason, it is important to determine the minerals that tend to precipitate in thermal waters and examine their equilibrium states under operation conditions.

The saturation indices of calcite, aragonite, dolomite, barite, gypsum, celestine, chalcedony and quartz minerals were calculated with the PhreeqC program (Ilnl.dat) [54] at the sampling temperature of the EGF thermal waters and the results are given in Fig. 7. Negative values indicate that the minerals are undersaturated and have a tendency to dissolve in water, while positive values imply that minerals are oversaturated and waters are likely to precipitate minerals of interest. Accordingly, all thermal waters tend to dissolve anhydrite and wairakite at discharge temperatures, and have a tendency to precipitate albite, aragonite, calcite, α -cristobalite, dolomite, gibbsite, illite, K-feldspar, kaolinite, laumontite, muscovite, paragonite, pyrophyllite, quartz and sanidine. The XRD analysis of two travertine samples was collected from the Kula area. Results of analysis yielded aragonite (in sample taken from a travertine ridge in the Emir Spa) and calcite (in sample collected around the TW-3 well).

To investigate the fluid–mineral equilibria in the Kula field, activity diagrams were constructed at temperatures of 75 and 125 °C for K_2O – Al_2O_3 – SiO_2 – H_2O and Na_2O – K_2O – Al_2O_3 – SiO_2 – H_2O systems, involving kaolinite, muscovite, K-feldspar, albite and gibbsite (Fig. 8). We used the SUPCRT-92 computer program [55] to estimate the equilibrium constants (K_{eq}) of the reactions between these minerals, which have common boundaries in the activity diagrams [56].

In the calculations, activities of water (a_{H_2O}) and minerals were assumed unity (1), and the activity of silicic acid ($a_{H_4SiO_4}$) or SiO_2 was fixed at the average silica concentration of the EGF thermal waters ($\log a_{H_4SiO_4} = -2.78$). The activities of Na^+ , K^+ , H_4SiO_4 and H^+ were estimated with the PhreeqC program [54] and plotted on the same diagrams. As suggested by the previous studies [56, 57], the activities of the dissolved species do not considerably change as the temperature of the solution varies, unlike the stability fields of minerals. In other words, locations of the samples in the diagrams remain the same. Water samples show an equilibrium tendency between muscovite and K-feldspar (Fig. 8). Therefore, high Na^+ and K^+ concentrations in the EGF thermal waters are attributed to the dissolution of silicate minerals, including muscovite, K-feldspar and albite.

4.3 Isotope Compositions

4.3.1 Oxygen–Hydrogen Isotopes

Stable oxygen ($\delta^{18}O$) and hydrogen (δD) isotopes are effective tracers used to determine the origin (meteoric, fossil and metamorphic) and recharge areas of geothermal fluids and the former is a widely used tool for estimating the fluid temperature in the aquifer. Isotope composition of the precipitation (snow or rain) is very crucial for the assessment of isotope systematics of groundwater. Variations in the isotopic composition of rainwater are related to the condensation process occurring at different temperatures during the movement of water vapor in the atmosphere. Since isotopic data are not available for precipitation in the EGF, we used the data recorded at the İzmir meteorological station 150 km west of the study area. $\delta^{18}O$ and δD values of precipitation in Izmir are -2.62 to -10.56‰ (SMOW) (average -4.80‰) and -24.81 to -74.17‰ (SMOW) (average -27.63‰) [58]. Local rainwater has a lower isotopic composition with $\delta^{18}O$

Fig. 7 Saturation index of minerals in the thermal waters

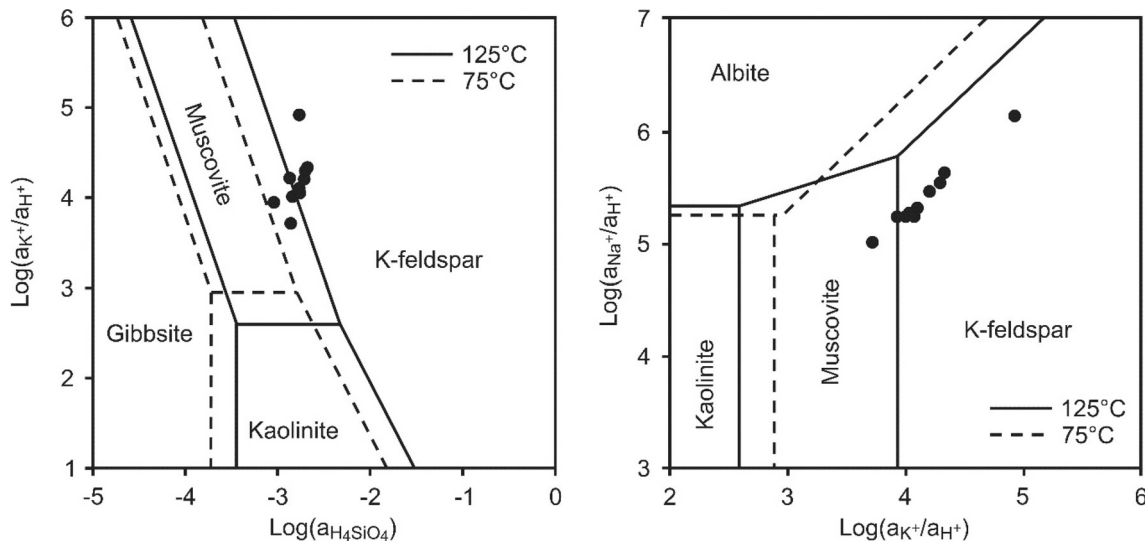
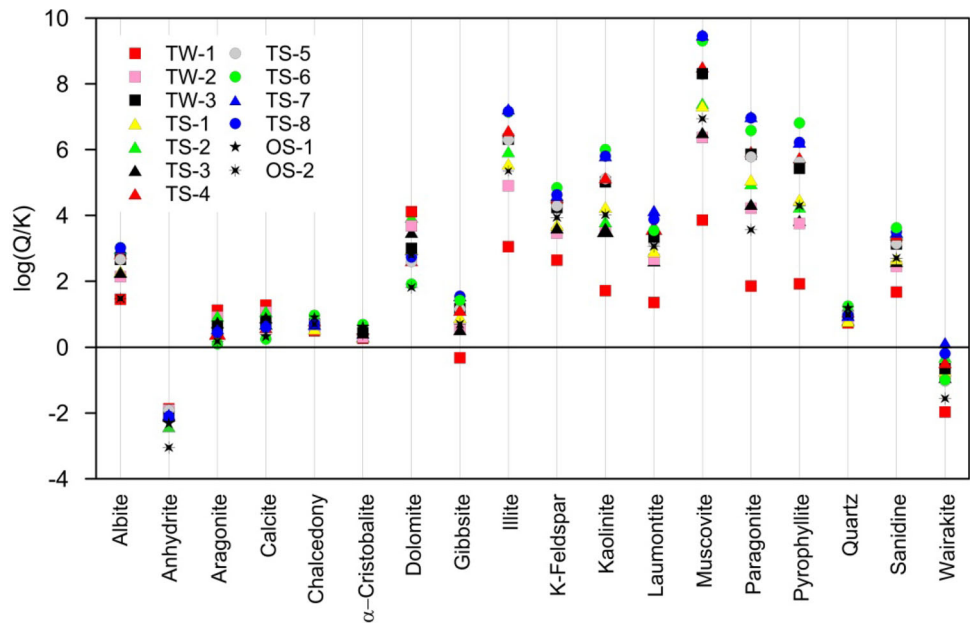


Fig. 8 Activity diagrams for thermal waters from the EGF at 75 and 125 °C in the systems of $K_2O-Al_2O_3-SiO_2-H_2O$ and $Na_2O-K_2O-Al_2O_3-SiO_2-H_2O$

of -9.98‰ and δD of -66.51‰ (Table 2). Because isotopic fractionation between atmospheric water and water vapor is more significant at low temperatures, water vapor moving inland and toward high, cold regions is depleted in heavy isotopes. Cloud masses with repeated and increasingly colder precipitation moving from the Aegean Sea to Kula would have more negative isotope values. Environmental isotope values of Izmir precipitation are accepted as local rainfall values and assessment of data was made using Global Meteoric Water Line (GMWL, $\delta D = 8 \times \delta^{18}O + 10$ [59]) and Local Meteoric Water Line (LMWL) defined by Dilaver et al. [58] ($\delta D = 8 \times \delta^{18}O + 11.99$).

$\delta^{18}O$ values of the EGF thermal waters vary from -9.4 to -8.41‰ and those of orthothermal and cold waters are between -7.56 and -5.89‰ (VSMOW) (Table 2). δD of thermal waters is from -64.16 to -56.38‰ (VSMOW) which are lower than that of orthothermal and cold waters (-50.70 to -44.10‰). Oxygen-hydrogen isotope systematics of thermal waters are significantly higher than cold waters. In the $\delta^{18}O$ - δD diagram (Fig. 9), samples plot between the GMWL and LMWL. Thermal waters and rainwater with lower isotope contents (depleted in heavy isotopes) indicate recharge from relatively higher elevations. However, cold waters with higher isotope contents (depleted in light isotopes) are probably recharged from lower elevations.

Table 2 Results of isotope analysis

No	$\delta^{18}\text{O}$ (‰VSMOW)	δD (‰VSMOW)	T (TU)	$\delta^{13}\text{C}$ (‰VPDB)	$\delta^{34}\text{S}$ (SO ₄) (‰VCDT)	$\delta^{18}\text{O}$ (SO ₄) (‰VSMOW)
TW-1	-9.40 ± 0.35	-64.16 ± 0.78	0.62 ± 0.41	1.70		
TW-2	-9.20 ± 0.32	-62.87 ± 0.75		2.38	39.89	10.84
TW-3	-9.04 ± 0.13	-62.17 ± 1.38	0.00 ± 0.35	3.12		
TS-1	-9.01 ± 0.32	-60.58 ± 0.79	0.68 ± 0.38	2.27	34.58	8.97
TS-2	-8.91 ± 0.13	-59.69 ± 1.38	2.38 ± 0.46	1.32	34.65	8.80
TS-3	-9.35 ± 0.16	-63.43 ± 1.40	0.90 ± 0.44	2.35		
TS-4	-8.51 ± 0.13	-56.38 ± 1.38		3.40		
TS-5	-9.02 ± 0.13	-62.98 ± 1.38	0.93 ± 0.44	3.79		
TS-6	-8.41 ± 0.14	-60.43 ± 1.38	1.80 ± 0.45	4.46		
TS-7	-8.87 ± 0.13	-61.28 ± 1.40	0.35 ± 0.38	2.84		
TS-8	-8.51 ± 0.14	-60.88 ± 1.38	0.33 ± 0.42	2.67		
OS-1 ^a	-7.54	-50.70				
OS2	-5.89 ± 0.09	-42.83 ± 0.73	1.63 ± 0.53	-11.61		
CS-1	-7.09 ± 0.14	-44.10 ± 1.39	5.97 ± 0.53	-10.02		
CS-2	-7.56 ± 0.13	-47.10 ± 1.38	5.34 ± 0.53	-2.33		
RW	-9.98 ± 0.09	-66.51 ± 0.73	8.79 ± 0.52			

^a[27]; blank: not analyzed

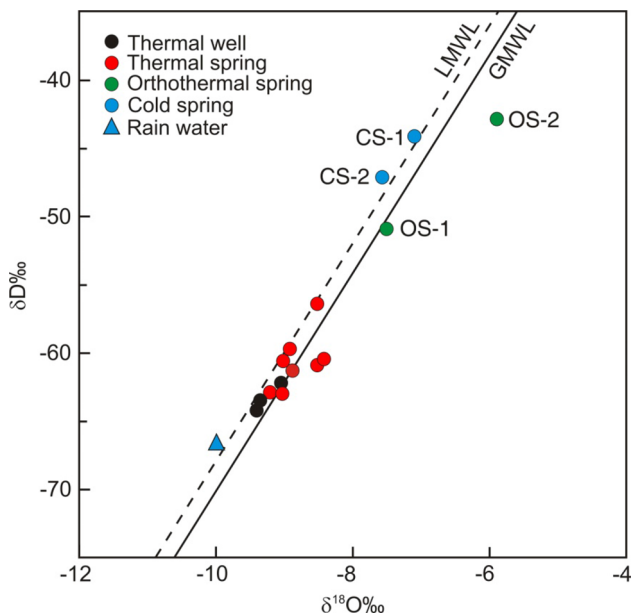


Fig. 9 $\delta^{18}\text{O}$ vs. $\delta^2\text{H}$ diagram for the EGF thermal and cold waters

The relative moisture that originates from the evaporative source of the vapor has a great effect on deuterium excess in meteoric water [60, 61]. Deuterium excess in the EGF thermal waters (except for TS-6) varies from 9.62 to 11.7‰ (average 10.66‰) and it is in the range of 4.29–13.38‰ for the orthothermal and cold waters. These values are consistent with the array proposed for the Aegean Sea (13–17‰

[62]), and therefore, it can be postulated that EGF, like other geothermal fields in the region (e.g., Hisaralan geothermal field [63]), is recharged by precipitation originating from the moisture of the Aegean Sea. The O–H isotope systematics show that OS-2 spring water is under the influence of surface evaporation (Fig. 9).

4.3.2 Tritium

Tritium values measured during the 2012–2016 years from the İzmir precipitation are between 1.96 and 11.54 TU ($n = 38$, mean = 4.30, median = 3.52), with the values exceeding 8 TU are accepted as extreme ($n = 4$) [58]. Local rainwater has tritium content of 8.79 TU (Table 2). The tritium concentration of precipitation tends to increase with altitude and distance from the coast to the inland [64]. For this reason, tritium content of rainfall recharging the EGF is expected to be higher than the İzmir precipitation. Tritium values of the EGF waters are from 0 to 5.97 TU with ranges of 0–2.38 TU for thermal and orthothermal waters and 5.34–5.97 TU for the cold waters (Table 2). Tritium of thermal waters, except for TS-2 and TS-6, is less than 1 indicating a deep circulation. In other words, they point to recharge prior to 1952 (< 0.8 TU [65]). The tritium values of TS-2 and TS-6 thermal and OS-2 orthothermal spring waters imply mixing between sub-modern and modern recharge ($0.8 > \text{TU} > \sim 4$ [65]).

The tritium values for CS-1 and CS-2 springs suggest a significant contribution from recent precipitation (5–15 TU, < 5–10 years [65]).

4.3.3 Carbon Isotopes and Sources

Carbon in the waters could originate from a number of sources, which include limestone, mantle, organic material and the atmosphere. The isotope composition of these carbon reservoirs varies in a wide range, from -30‰ for coal to 0‰ for the marine limestone and even up to 10‰ for metamorphic CO_2 [65]. Carbon isotope composition ($\delta^{13}\text{C}$) measured in dissolved inorganic carbon (DIC) range from 1.32 to 4.46‰ for thermal waters and -11.6 to -2.33‰ for the cold and orthothermal waters (Table 2). In previous studies, $\delta^{13}\text{C}(\text{CO}_2)$ of OS-1 is reported -6.6‰ [75] and $\delta^{13}\text{C}(\text{CO}_2)$ values of TS-3 spring are given in the range of -5.0‰ [66] to -1.60‰ [67]. These values are lower than our measurements ($+1.32$ to $+4.46\text{‰}$).

In order to determine the endogenous CO_2 contribution to the $\delta^{13}\text{C}(\text{DIC})$ values of waters, the $\delta^{13}\text{C}_{\text{ext}}(\text{CO}_2)_{\text{aq}}$ value should be known. $\delta^{13}\text{C}$ of deep CO_2 ($\delta^{13}\text{C}_{\text{ext}}$) in water samples was calculated from the following isotope-mass balance [68]:

$$\delta^{13}\text{C}(\text{DIC}) \times \text{DIC} = (\delta^{13}\text{C}_{\text{carb}} \times \text{C}_{\text{carb}}) + (\delta^{13}\text{C}_{\text{ext}} \times \text{C}_{\text{ext}}) \quad (11)$$

C_{carb} and C_{ext} are estimated from the succeeding equations [68]:

$$\text{DIC} = \text{C}_{\text{carb}} + \text{C}_{\text{ext}} \quad (12)$$

$$\text{C}_{\text{carb}} = \text{Ca} + \text{Mg} - \text{SO}_4 \quad (13)$$

$$\text{C}_{\text{ext}} = \text{DIC} - \text{C}_{\text{carb}} = \text{C}_{\text{inf}} + \text{C}_{\text{deep}} \quad (14)$$

where C_{carb} stands for carbon that is derived from interaction of groundwater with carbonate reservoir rocks, C_{ext} derived from external sources, C_{inf} represents atmospheric and biogenic CO_2 , and C_{deep} stands for metamorphic, mantle or magma-derived carbon. Molality values of DIC, Ca, Mg and SO_4 were computed PhreeQC (Ilnl.dat) program.

DIC and C_{ext} molalities of are found $4.19\text{E}-02$ to $7.30\text{E}-02$ and $3.93\text{E}-02$ to $6.56\text{E}-02$ mol/kg. Molality values of OS-2 and cold waters are estimated as $1.62\text{E}-02$ to $5.48\text{E}-03$ and $1.14\text{E}-02$ to $3.11\text{E}-02$ mol/kg, respectively. $\text{C}_{\text{ext}}/\text{DIC}$ ratios are from 0.89 to 0.94 for thermal waters and 0.47 to 0.71 for other waters, indicating that C_{ext} contribution to thermal waters is higher than cold waters. $\delta^{13}\text{C}$ of marbles in the Menderes massif is reported to range from 0.21 to 3.94‰ (average 2.92‰ [69]). Using the average $\delta^{13}\text{C}$ value

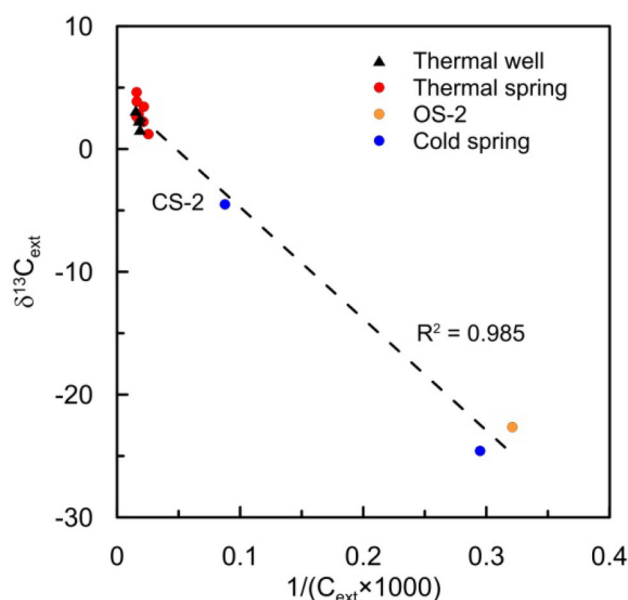


Fig. 10 $\delta^{13}\text{C}_{\text{ext}}$ vs. $1/(\text{C}_{\text{ext}} \times 1000)$ diagram for the EGF waters

of Menderes massif marbles, $\delta^{13}\text{C}_{\text{ext}}$ of thermal waters is estimated 1.59 to 4.61‰ which are very close to $\delta^{13}\text{C}(\text{DIC})$ of thermal waters showing a strong positive correlation ($R^2 = 0.99$). $\delta^{13}\text{C}_{\text{ext}}$ values estimated for OS-2 and cold springs are almost twice as negative as the $\delta^{13}\text{C}(\text{DIC})$ values of these waters (OS-2: -22.65‰ , CS-1: -24.59‰ , CS-2: -4.52‰). $\delta^{13}\text{C}_{\text{ext}}$ calculated from the model of Chiodini et al. [68] and NetpathXL code [70] are reported very similar (mean difference: $\pm 0.1\text{‰}$) [81]. For this reason, $\delta^{13}\text{C}_{\text{ext}}$ values of studied waters can be safely used as $\delta^{13}\text{C}_{\text{ext}}(\text{CO}_2)_{\text{aq}}$.

The $\delta^{13}\text{C}_{\text{ext}}$ vs. $1/(\text{C}_{\text{ext}} \times 1000)$ diagram (Fig. 10) [71] shows that $\delta^{13}\text{C}_{\text{ext}}$ values increase with the increase in C_{ext} values of waters and carbon in OS-2 and CS-1 spring waters is of biogenic origin while carbon in other waters is derived from deep sources. $\delta^{13}\text{C}(\text{DIC})$ values of thermal waters (Table 2) are more positive when compared with $\delta^{13}\text{C}(\text{CO}_2)_{\text{g}}$ of OS-1 (-6.6‰ [66]) and TS-3 (-1.6‰ , [67]). This might be attributed to enrichment of heavy carbon isotope (^{13}C) in the residual thermal waters due to degassing. Hence, we conclude that the DIC in the EGF thermal waters is mainly of deep origin.

4.3.4 Sulfur and Oxygen Isotopes of the Dissolved Sulfate

In natural waters, $\delta^{34}\text{S}$ values of sulfur species fall in a wide range from -50‰ to $+50\text{‰}$ (CDT). This variation is due abiotic and biotic redox processes in open and closed systems [72]. Therefore, the source of the sulfate in thermal waters might be highly variable. Dissolution of sulfates, oxidation of sulfides and organic matter are the major sources of sulfate. The modern seawater, another sulfate source, is represented by a homogeneous $\delta^{34}\text{S}$ value of $+20\text{‰}$ [73]. $\delta^{34}\text{S}$

of marine evaporites has varied between 10 and 30‰ during the Phanerozoic, with 20‰ for the Tertiary evaporites. For the non-marine evaporites, $\delta^{34}\text{S}$ and $\delta^{18}\text{O}$ of sulfate have the following ranges of -15 to 10 ‰ and -10 to 4 ‰. Magmatic sulfur has a rather narrow range of $+5$ to -5 ‰ [65].

The $\delta^{34}\text{S}$ of dissolved sulfate measured in selected thermal waters falls in the range of 34.5–39.9‰ (VCDT) and $\delta^{18}\text{O}$ varies from 8.8 to 10.8‰ (VSMOW) (Table 2). The $\delta^{34}\text{S}$ values are significantly higher than those of the various geological reservoirs, and in particular, higher than the values for the marine evaporites. Although rare, such high $\delta^{34}\text{S}$ values are recorded in geological environments. For example, Late Devonian evaporite deposits of the Souris River Formation in Canada are reported to have sulfur isotope values of >30 ‰ (maximum 34‰) [74, 75]. Likewise, high $\delta^{34}\text{S}$ values are also found in upper Triassic evaporite deposits (32.5‰ [76]) and in CAS of Late Devonian limestones (up to 32‰ [77]) in southern China. Finally, structurally substituted sulfate (SSS) on the Late Scythian and Early Anisian brachiopod crusts have $\delta^{34}\text{S}$ values of up to 29.7‰ [78].

Bacterial sulfate reduction results in an increase in ^{34}S (enrichment of heavy isotopes) in the residual sulfate [79]. For example, $\delta^{34}\text{S}$ of dissolved sulfate in the Murray basin of SW Australia is found to increase from 0 to 56.4‰ [80] and $\delta^{34}\text{S}$ of groundwater in Sturgeon Falls (Canada) is reported to have a value of 15.5‰ [81]. Bacterial reduction causes breaking of ^{16}O bonds, leaving the residual sulfate enriched in heavy oxygen isotope (^{18}O), and causing enrichment factors that are generally two–four times greater than that for the ^{34}S enrichment [82]. It is therefore suggested that oxidation of sulfides followed by bacterial sulfate reduction (as evidenced by the H_2S –rotten egg odor in springs) is the key mechanism behind the observed sulfate isotope systematics of the EGF samples.

4.4 Estimation of Reservoir Temperature

In this study, cation, silica, mineral equilibrium and isotope geothermometer methods were used to estimate the reservoir temperature of the EGF and the results are given in Table 3. In the evaluation of geothermometer results, the OS-2 spring was not taken into account as this sample yielded extreme reservoir temperatures (up to -20 and 381 °C).

4.4.1 Cation Geothermometers

Among the reservoir temperatures calculated with cation geothermometers, the highest values were obtained from Na–K (170–243 °C) and Na–K–Ca (181–202 °C) geothermometers. Reservoir temperatures estimated with other cation geothermometers yielded lower values spanning in a narrow range (K–Mg: 75–95 °C, Mg–Li: 46–71 °C and Na–Li: 80–98 °C). In this study, we use Na/400–K/10– $\sqrt{\text{Mg}}$

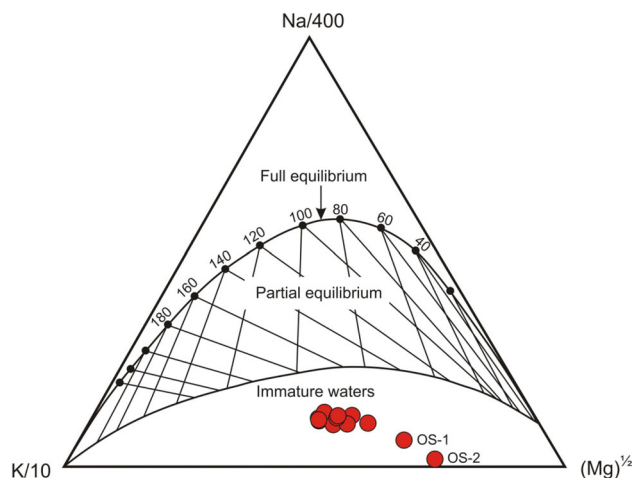


Fig. 11 Na/400–K/10– $\sqrt{\text{Mg}}$ diagram [91]

diagram of Giggenbach and Corrales [91], which is more suitable for the evaluation of equilibrium conditions at temperatures lower than 200 °C (Fig. 11). In this diagram, all samples plot into the “immature waters field,” suggesting that application of cation geothermometers may not be suitable for the estimation of subsurface temperatures. However, for near-neutral HCO_3 waters, such as the EGF waters, the K–Mg temperatures computed from Eq. (15) can be evaluated [91]:

$$t_{\text{km}} = [4410 / (14 - \log(C_{\text{K}}^2 / C_{\text{Mg}}))] - 273 \quad (15)$$

The reservoir temperatures estimated by this geothermometer are in the range of 75–95 °C (Fig. 11, Table 3), which are higher than the measured values. This might reflect that the interaction of thermal water with clays in the reservoir took place at high temperatures [91]. Due to the faster rate of equilibration between mineral and water, the K–Mg temperatures are significantly lower than the Na–K temperatures and likely reflect conditions less than around 150 °C at shallower levels [92]. Na–K geothermometers applied to the EGF thermal waters yielded very high temperatures (160–243 °C), which are considered unrealistic (Table 3). Similarly, high reservoir temperatures estimated by the Na–K–Ca geothermometer (181–202 °C) are not convincing due to possible dissolution/precipitation of carbonates at shallow depths.

Temperature estimates from the Mg–Li geothermometer (46–71 °C) are lower than both Na–Li and K–Mg geothermometers. However, Na–Li temperatures ($\text{Cl}^- < 0.3$ M; 80–98 °C) are very close to those estimated by the K–Mg geothermometers (Table 3).

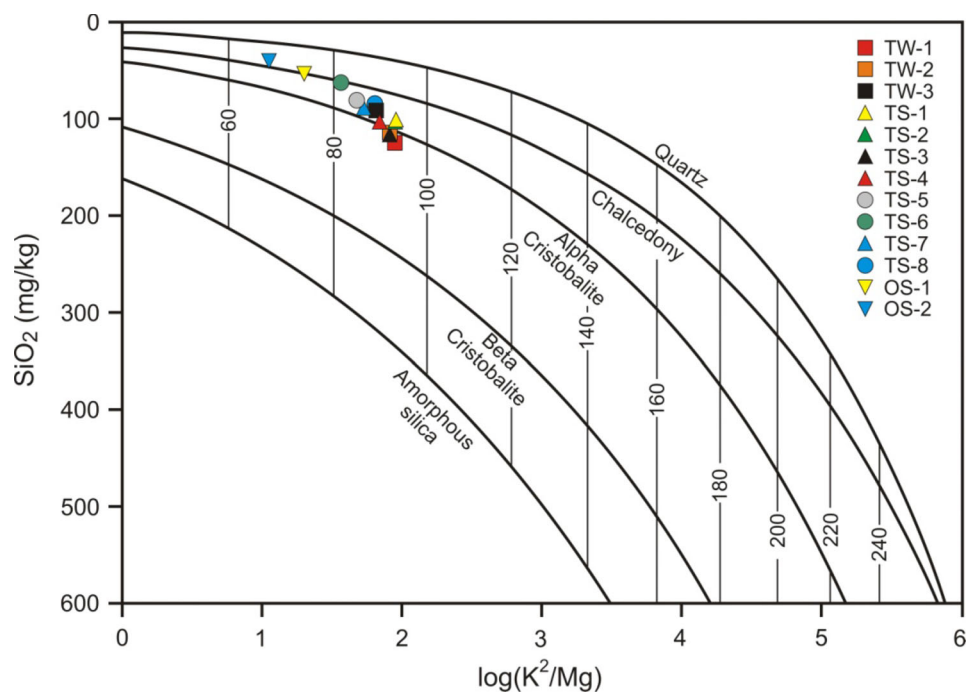


Table 3 Reservoir temperatures (°C) of the EGF thermal waters

No	T_{meas}	Na–K ^a	Na–K ^b	K–Mg ^c	Mg–Li ^d	Na–Li ^e	Na–K–Ca ^f	SiO ₂ ^g α-Crist	SiO ₂ ^g Chalc	SiO ₂ ^g Quartz	¹⁸ O(SO ₄ -H ₂ O) ^h
TW-1	63.3	179	226	94	71	94	195	100	125	150	
TW-2	56.6	180	227	93	68	91	195	94	119	145	83
TW-3	39.1	174	222	90	67	91	189	82	105	132	
TS-1	52.0	189	233	95	66	89	200	87	111	138	98
TS-2	41.1	182	228	94	68	89	202	88	112	139	100
TS-3	55.0	170	219	93	69	88	194	95	120	146	
TS-4	35.5	194	237	91	60	86	197	88	112	139	
TS-5	31.4	160	212	86	61	80	181	75	98	126	
TS-6	21.1	167	217	83	58	83	182	62	84	113	
TS-7	38.2	187	232	88	64	98	194	80	103	131	
TS-8	36.1	170	219	90	66	88	189	77	100	128	
OS-1	15.5	202	243	75	46	92	181	55	75	105	
OS-2	18.4	381	358	69	–20	–1	92	41	60	91	
*Mean		180	226	89	64	89	192	82	105	133	94

^a[83], ^b[84], ^c[85], ^d[86], ^e[87], ^f[88], ^g[89], ^h[90]; T_{meas} : measured temperature; blank: no data. *OS-2 is not included in the mean

Fig. 12 Cross-plot of the K–Mg and silica geothermometers for the EGF thermal waters [93]



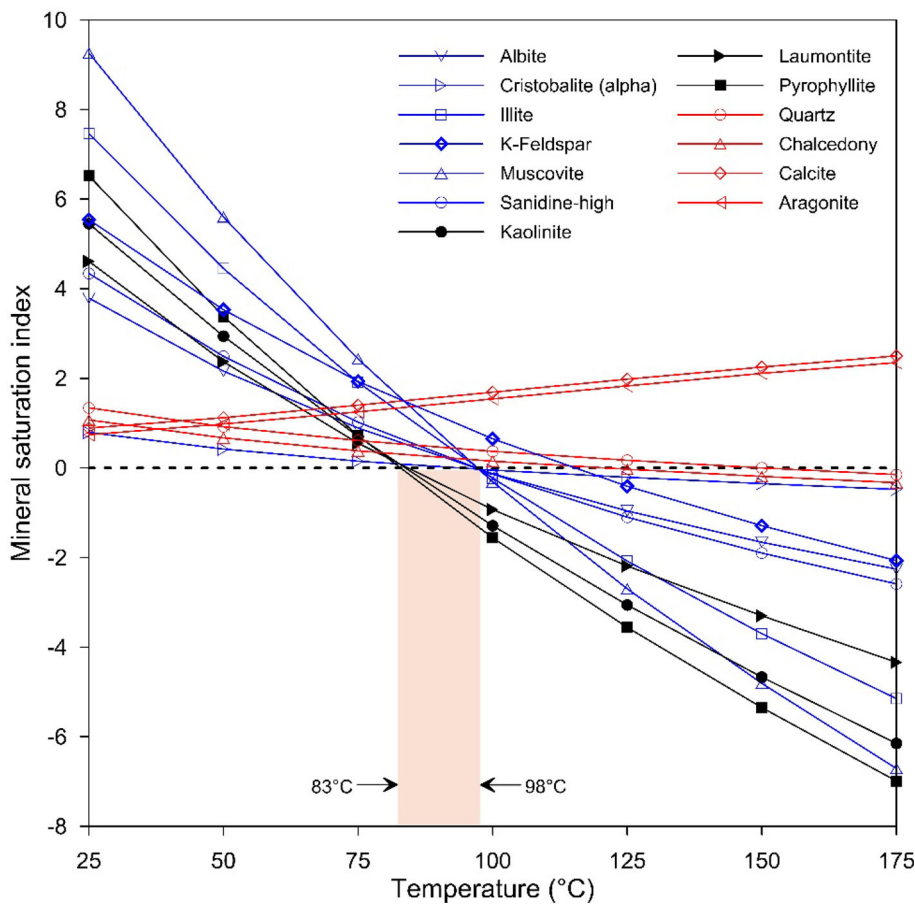
4.4.2 Silica Geothermometers

Reservoir temperatures of thermal and OS-1 waters estimated by the alpha cristobalite, chalcedony and quartz geothermometers are 55–100, 75–125 and 105–150 °C. An additional estimation of the reservoir temperature was made using the cross-plot of K–Mg and the quartz (conductive) geothermometer [93] (Fig. 12). This method is usually accepted to be more suitable than individual quartz or K–Mg-based geothermometers for waters derived from a

lower-temperature source. Because the diagram combines two low-temperature geothermometers, it gives relatively more reliable temperature estimates than quartz or K/Mg-based geothermometers [94]. The solubility curve of SiO₂ indicates the dissolution state of minerals and which mineral controls the silica content in the solution. Figure 12 shows that studied thermal waters plot in between cristobalite and chalcedony curves and they achieve equilibrium at temperatures below 95 °C.



Fig. 13 Saturation diagram constructed for sample TW-1 at temperature of range of 25–175 °C



4.4.3 Mineral Equilibrium Diagram

The reservoir temperature of the EGF is further assessed by the saturation state calculations at different temperatures. This model considers the saturation states of selected minerals that were estimated with the PhreeqC program [54]. When a group of minerals is close to the equilibrium line (SI = 0) at a specific temperature, it is assumed that the water is equilibrated with these minerals and the temperature reflects the reservoir temperature [56]. Mineral equilibrium diagram in Fig. 13 implies that reservoir temperature determined for sample TW-1 (83–98 °C) is consistent with temperature estimations from geothermometers.

4.4.4 Sulfate-Water Isotopic Geothermometer

Using the equation proposed by Lloyd [90], reservoir temperature of selected waters (TW-2, TS-1 and TS-2) is computed in the range of 83 to 100 °C (Table 3). These temperatures are highly consistent with the results obtained from K–Mg, Na–Li, chalcedony geothermometers and mineral equilibrium diagram. This geothermometer has been successfully used for a number of water-dominated geothermal systems at temperatures of 100–350 °C [79, 95, 96]. Low reservoir

temperatures require long residence time to achieve isotopic equilibrium (e.g., 500 years at 100 °C) which makes geothermometer estimates inappropriate to low-temperature reservoirs unless residence time of waters is exceptionally prolonged [97]. Although no radiocarbon age data is available for the EGF thermal waters, tritium values indicate pre-1952 recharge. For this reason, assessments of geothermometer results should be made cautiously. However, application of ¹⁸O(SO₄–H₂O) geothermometer to the low-enthalpy fields might be useful to verify the chemical geothermometer results [98].

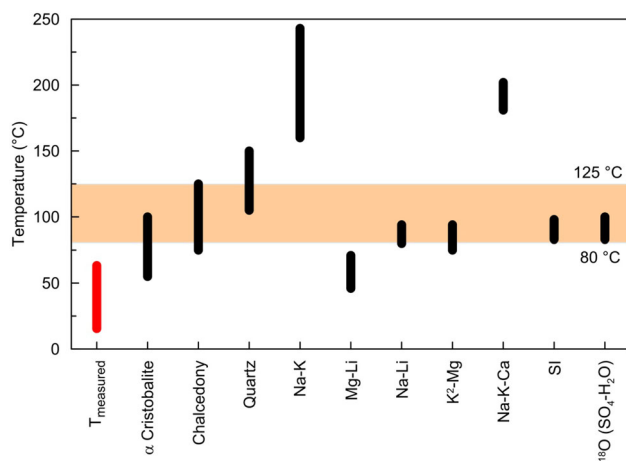
Figure 14 summarizes the temperature ranges estimated from several geothermometer models. The expected reservoir temperature for the EGF thermal waters is 80–125 °C. Considering that the annual average atmospheric temperature in the region is 14.8 °C and geothermal gradient is 93.4 °C/km [26], the circulation depth of thermal waters is estimated to be 700–1200 m.

4.5 Fossil Fluid Circulation

We collected travertine samples from bedded travertine deposits along the Geren Creek (samples 1–5) and from a fissure ridge at southern part of Emir Spa (samples 6–9; Fig. 1c).

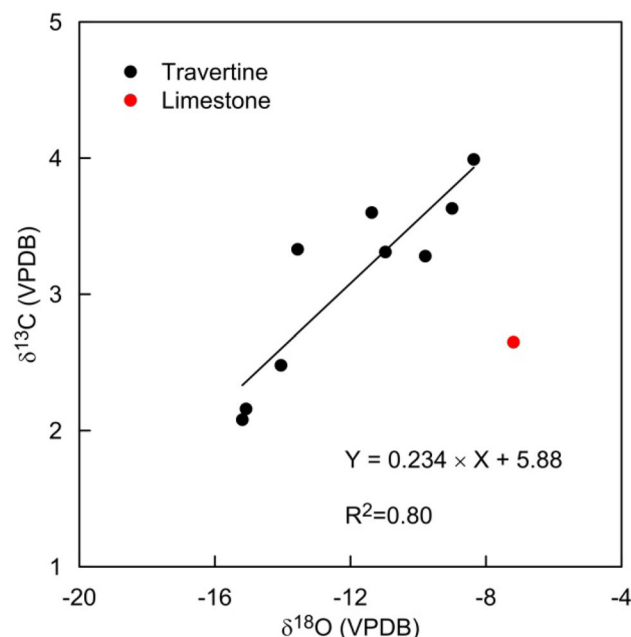
Table 4 Results of stable isotope analyses of Kula travertines and paleo-temperatures estimated by various oxygen isotope fractionation calibrations

No	$\delta^{13}\text{C}(\text{‰})$ VPDB	$\delta^{18}\text{O}(\text{‰})$ VPDB	$\delta^{18}\text{O}(\text{‰})$ SMOW	Paleo-temperature ($^{\circ}\text{C}$)		
				Friedmann and O'Neil [99]	Kim and O'Neil [100]	Kele et al. [101]
1	3,31	- 10.97	19.60	24.3	22.7	34.5
2	3,28	- 9.79	20.82	18.7	16.9	28.9
3	3,99	- 8.36	22.29	12.3	10.2	22.3
4	3,63	- 9.00	21.63	15.1	13.1	25.2
5	3,60	- 11.37	19.19	26.3	24.7	36.5
6	3,33	- 13.56	16.93	37.8	36.2	47.7
7	2,16	- 15.08	15.36	46.6	44.8	56.0
8	2,08	- 15.19	15.25	47.3	45.4	56.6
9	2,48	- 14.05	16.42	40.6	38.9	50.3
10	2,65	- 7.19	23.37			

**Fig. 14** Comparison of calculated geothermometers estimated for the EGF thermal waters

Mesozoic limestone (sample no 10) exposed within the study area was also sampled for comparison of stable isotope compositions (Table 4). The carbon isotope composition of Emir travertines is in the range of 2.08–3.99‰ (VPDB) and $\delta^{18}\text{O}$ values are from - 15.19 to - 8.36‰ (VPDB). The Mesozoic limestone in the region is represented by $\delta^{13}\text{C}$ of 2.65‰ (VPDB) and $\delta^{18}\text{O}$ of - 7.19‰ (VPDB). $\delta^{13}\text{C}$ compositions of travertine samples with an average of 3.1‰ are consistent with marine limestone ($\pm 3\text{‰}$ [65]). Carbon isotope contents of travertines are quite similar to the EGF thermal waters (from 1.32 to 4.46‰), but considerably higher than cold springs (- 11.61 to - 2.33‰). The negative values indicate that organic carbon significantly contributes to the carbon composition of cold waters.

In the $\delta^{13}\text{C}$ vs. $\delta^{18}\text{O}$ diagram (Fig. 15), except for the limestone sample, carbon-oxygen isotope contents of Emir travertines are strongly correlated ($R^2 = 0.8$). The robust

**Fig. 15** $\delta^{13}\text{C}$ vs. $\delta^{18}\text{O}$ diagram for Kula travertine samples

positive correlation is attributed to kinetic isotope fractionation induced by the preferential degassing of lighter $^{12}\text{CO}_2$ [102]. As shown by Fig. 15, oxygen isotope values also increase with increase in $\delta^{13}\text{C}$ which might be modified by preferential evaporation of H_2^{16}O . This process results in a consequent increase in $\delta^{18}\text{O}$ of the precipitated calcite [103]. CO_2 degassing is a common process in regions of volcanic and tectonic unrest. Previous studies indicate that volatile budget of geothermal fluids in the western Anatolia is greatly enriched in CO_2 and helium [10, 104]. Helium isotope composition of dissolved gases collected from OS-1 and TS-3 are reported 2.82 and 1.71 R/R_A (where $R = \text{sample } ^3\text{He}/^4\text{He}$

and $R_A = \text{air } ^3\text{He}/^4\text{He}$) [67, 104]. These values yield significant amount of mantle-derived He (approximately 35% of the total helium inventory) in the thermal waters accompanied by high CO_2 concentrations.

Carbon isotope composition of CO_2 in gas samples in the Kula area is reported in the range of -6.6 to -1.60% [66, 67], which corresponds to marine limestone (-3 to $+3\%$ [65]). Carbon in waters is probably derived from the dissolution of marbles within the Menderes Massif that comprise the basement lithology in most parts of the western Turkey. In a study by Mutlu et al. [10], a quantitative assessment was made for the carbon inventory in gas samples collected from the western Turkey. Results indicated that carbon derived from the marine limestone is the principal contributor to the carbon budget, followed by organic carbon and endogenic (mantle-derived) carbon. Helium, however, is most likely transferred to the crust by fluid degassing from mantle melts that were generated by current extensional tectonics in the region [104].

Oxygen isotope compositions of travertines (15.25 – 22.29% VSMOW) are considerably higher than thermal waters (-9.40 to -8.41% VSMOW) probably because of surface evaporation (Tables 2 and 4). Oxygen isotopes are useful tool to estimate the isotope composition and/or equilibrium temperature of waters at which travertine has precipitated [99]. Oxygen isotope fractionation between carbonate phase and water ($\Delta^{18}\text{O}_{\text{calcite-water}}$) is the most commonly used technique for the calculation of paleo-temperatures of carbonates [100, 101]. Assigning an average value of -8.93% for the $\delta^{18}\text{O}$ of the EGF thermal waters, it is possible to estimate the paleo-temperature of calcite-depositing water. We applied several calibrations and the results are shown in Table 4. Temperatures estimated by equations of Friedmann and O'Neil [99] and Kim and O'Neil [100] yielded lower ranges of 12.3 – 47.3 and 10.2 – 45.4 °C, respectively. Another calibration proposed by Kele et al. [101] (22.3 – 56.6 °C) resulted in temperatures which are almost 10 °C higher than previous estimates. High temperatures estimated using $\delta^{18}\text{O}$ values of the fissure ridge travertines well agree with temperatures of well waters (56.6 – 63.3 °C; Table 1), given that discharge temperatures of thermal waters in the study area have not noticeably changed since the precipitation of travertines.

5 Conclusion

Metamorphics of the Menderes massif, Mesozoic limestones and porous and permeable lithologies of the Vezirler mélange are the reservoir rocks of the EGF thermal waters. Impermeable units of Neogene comprise the cap rocks. High geothermal gradient associated with neotectonic activity is the heat source of geothermal system. The studied waters

have a meteoric origin that are recharged by precipitation sourced from the Aegean Sea. Thermal waters with tritium values less than 1 TU imply recharge of prior to 1952.

Thermal waters in the EGF are Na- HCO_3 type and have temperatures between 21.1 and 63.3 °C. Chemical composition of waters is controlled by several processes that include water–rock interaction, dissolution/precipitation and ion exchange reactions. Stable isotope systematics indicate that carbon in waters is derived from marine carbonate rocks and endogenic sources while sulfur originates from bacterial sulfate reduction and dissolution of marine carbonates (CAS) and sulfide minerals.

Chalcedony, K–Mg, Mg–Li, Na–Li, mineral equilibrium diagram and $\delta^{18}\text{O}(\text{SO}_4\text{--H}_2\text{O})$ isotope geothermometers applied to the EGF thermal waters yielded similar reservoir temperatures varying from 80 to 125 °C. Paleo-temperatures of calcite-forming waters estimated using $\delta^{18}\text{O}$ values of travertines are consistent with discharge temperatures of the EGF thermal springs.

The EGF thermal waters are utilized as spa, but temperature and discharge of geothermal waters are also suitable for greenhouse heating. Apart from this, if boreholes with depth exceeding 1000 m are opened in the EGF, it is highly probable that the temperature and flow rate of the geothermal fluid will be suitable for integrated use, and especially for the electricity production.

Acknowledgements This study was financially supported by the Scientific Research Coordination Unit of Pamukkale University [Grant No. 2018FEBE049]. Prof. Mehmet Özkul, Hüseyin Tosun of Kula Mayor and geological engineer Nuran Sevimli Akkoç are greatly acknowledged for their kindly support at every stage of the study. Authors appreciate the supportive comments of two anonymous reviewers and the subject editor, which greatly improved the manuscript.

Funding Open access funding provided by the Scientific and Technological Research Council of Türkiye (TÜBİTAK).

Open Access This article is licensed under a Creative Commons Attribution 4.0 International License, which permits use, sharing, adaptation, distribution and reproduction in any medium or format, as long as you give appropriate credit to the original author(s) and the source, provide a link to the Creative Commons licence, and indicate if changes were made. The images or other third party material in this article are included in the article's Creative Commons licence, unless indicated otherwise in a credit line to the material. If material is not included in the article's Creative Commons licence and your intended use is not permitted by statutory regulation or exceeds the permitted use, you will need to obtain permission directly from the copyright holder. To view a copy of this licence, visit <http://creativecommons.org/licenses/by/4.0/>.

References

- Şengör, A.M.C.; Yılmaz, Y.: Tethyan evolution of Turkey—a plate tectonic approach. *Tectonophysics* **75**, 181–241 (1981). [https://doi.org/10.1016/0040-1951\(81\)90275-4](https://doi.org/10.1016/0040-1951(81)90275-4)



2. Dewey, J.F.; Şengör, A.M.C.: Aegean and surrounding regions: complex multiplate and continuum tectonics in a convergent zone. *Geol. Soc. Am. Bull. Part 1* **90**, 84–92 (1979)
3. Bozkurt, E.: Neotectonics of Turkey—a synthesis. *Geodin. Acta* **14**, 3–30 (2001). <https://doi.org/10.1080/09853111.2001.11432432>
4. Güleç, N.T.; Hilton, D.R.: Helium and heat distribution in western Anatolia, Turkey: Relationship to active extension and volcanism. In: Dilek, Y., Pavlides, S. (eds.) *Post-collisional Tectonics and Magmatism in the Mediterranean Region and Asia*, Geological Society of America Special Papers, vol. 409, pp. 305–319 (2006). [https://doi.org/10.1130/2006.2409\(16\)](https://doi.org/10.1130/2006.2409(16))
5. Yılmaz, Y.: Comparison of the young volcanic associations of the west and the east Anatolia under the compressional regime: a review. *J. Volcanol. Geotherm. Res.* **44**, 69–87 (1990). [https://doi.org/10.1016/0377-0273\(90\)90012-5](https://doi.org/10.1016/0377-0273(90)90012-5)
6. Güleç, N.: Crust–mantle interaction in western Turkey: implications from Sr and Nd isotope geochemistry of Tertiary and Quaternary volcanics. *Geol. Mag.* **128**, 417–435 (1991). <https://doi.org/10.1017/S0016756800018604>
7. Mutlu, H.; Güleç, N.: Hydrogeochemical outline of thermal waters and geothermometry applications in Anatolia, Turkey. *J. Volcanol. Geotherm. Res.* **85**, 495–515 (1998). [https://doi.org/10.1016/S0377-0273\(98\)00068-7](https://doi.org/10.1016/S0377-0273(98)00068-7)
8. Akkuş, İ.; Akıllı, H.; Ceyhan, S.; Dilemre, A.; Tekin, Z.: Potential of Geothermal Resources of Turkey. MTA Book Series, vol. 201. Ankara (2005)
9. Ulusoy, İ.; Sarıkaya, M.A.; Schmitt, A.K.; Şen, E.; Danişık, M.; Gümüş, E.: Volcanic eruption eye-witnessed and recorded by pre-historic humans. *Quat. Sci. Rev.* **212**, 187–198 (2019). <https://doi.org/10.1016/j.quascirev.2019.03.030>
10. Mutlu, H.; Güleç, N.; Hilton, D.R.: Helium-carbon relationships in geothermal fluids of western Anatolia, Turkey. *Chem. Geol.* **247**, 305–321 (2008). <https://doi.org/10.1016/j.chemgeo.2007.10.021>
11. Ercan, T.; Türkecan, A.; Dinçel, A.; Günay, E.: Kula-Selendi (Manisa) dolaylarının jeolojisi. *Jeoloji Mühendisliği Dergisi* **17**, 3–28 (1983)
12. Ercan, T.: Kula yöresinin jeolojisi ve volkanitlerin petrolojisi. *İstanbul Yerbilimleri Dergisi* **3**, 77–124 (1982)
13. Innocenti, F.; Agostini, S.; Di Vincenzo, G.; Doglioni, C.; Manetti, P.; Savaşçın, M.Y.; Tonarini, S.: Neogene and Quaternary volcanism in Western Anatolia: Magma sources and geodynamic evolution. *Mar. Geol.* **221**, 397–421 (2005). <https://doi.org/10.1016/j.margeo.2005.03.016>
14. Borsi, S.; Ferrara, G.; Innocenti, F.; Mazzuoli, R.: Geochronology and petrology of recent volcanics in the Eastern Aegean Sea (West Anatolia and Lesvos Island). *Bull. Volcanol.* **36**, 473–496 (1972). <https://doi.org/10.1007/BF02597122>
15. Westaway, R.; Guillou, H.; Yurtmen, S.; Beck, A.; Bridgland, D.; Demir, T.; Scaillet, S.; Rowbotham, G.: Late Cenozoic uplift of western Turkey: improved dating of the Kula Quaternary volcanic field and numerical modelling of the Gediz river terrace staircase. *Glob. Planet. Chang.* **51**, 131–171 (2006). <https://doi.org/10.1016/j.gloplacha.2006.02.001>
16. Heineke, C.; Niedermann, S.; Hetzel, R.; Akal, C.: Surface exposure dating of Holocene basalt flows and cinder cones in the Kula volcanic field (Western Turkey) using cosmogenic ^3He and ^{10}Be . *Quat. Geochronol.* **34**, 81–91 (2016). <https://doi.org/10.1016/j.quageo.2016.04.004>
17. Seyitoğlu, G.; Scott, B.C.: The age of the Büyük Menderes Graben (west Turkey) and its tectonic implications. *Geol. Mag.* **129**, 239–242 (1992). <https://doi.org/10.1017/S001675680000830X>
18. McKenzie, D.; O’Nions, R.K.: The source regions of Ocean Island Basalts. *J. Petrol.* **36**, 133–159 (1995). <https://doi.org/10.1093/ptrology/36.1.133>
19. Yılmaz, Y.; Genç, S.C.; Gürer, O.F.; Bozcu, M.; Yılmaz, K.; Karacık, Z.; Altunkaynak, S.; Elmas, A.: When did the western Anatolian grabens begin to develop? In: Bozkurt, E.; Winchester, J.A.; Piper, J.D.A. (Eds.) *Tectonics and Magmatism in Turkey and the Surrounding Area*, Vol. 173, pp. 353–384. Geological Society Special Publication, London (2000). <https://doi.org/10.1144/GSL.SP.2000.173.01.17>
20. Hetzel, R.; Ring, U.; Akal, C.; Troesch, M.: Miocene NNE directed extensional unroofing of the Menderes Massif, Southwestern Turkey. *J. Geol. Soc. Lond.* **152**, 639–654 (1995). <https://doi.org/10.1144/gsjgs.152.4.0639>
21. Koçyiğit, A.; Yusufoglu, H.; Bozkurt, E.: Evidence from the Gediz Graben for episodic two-stage extension in Western Turkey. *J. Geol. Soc.* **156**, 605–616 (1999). <https://doi.org/10.1144/gsjgs.156.3.0605>
22. Seyitoğlu, G.; Tekeli, O.; Çemen, İ.; Şen, Ş.; Işık, V.: The role of the flexural rotation/rolling hinge model in the tectonic evolution of the Alaşehir graben, Western Turkey. *Geol. Mag.* **139**, 15–26 (2002). <https://doi.org/10.1017/S0016756801005969>
23. Bozkurt, E.: Granitoid rocks of the southern Menderes massif (southwestern Turkey): field evidence for Tertiary magmatism in an extensional shear zone. *Int. J. Earth Sci.* **93**, 52–71 (2004). <https://doi.org/10.1007/s00531-003-0369-0>
24. İlkışık, O.M.: Regional heat flow in western Anatolia using silica temperature estimates from thermal springs. *Tectonophysics* **244**, 175–184 (1995). [https://doi.org/10.1016/0040-1951\(94\)00226-Y](https://doi.org/10.1016/0040-1951(94)00226-Y)
25. Akın, U.; Ulugergerli, E.U.; Kutlu, S.: The assessment of geothermal potential of Turkey by means of heat flow estimation. *Bull. Min. Res. Exp.* **149**, 205–214 (2014)
26. Bilim, F.; Akay, T.; Aydemir, A.; Koşaroglu, S.: Curie point depth, heat-flow and radiogenic heat production deduced from the spectral analysis of the aeromagnetic data for geothermal investigation on the Menderes Massif and the Aegean region, western Turkey. *Geothermics* **60**, 44–57 (2016). <https://doi.org/10.1016/j.geothermics.2015.12.002>
27. Tokçaeer, M.: Geochemistry of Kula Geothermal Area. M.Sc. Thesis, Dokuz Eylül University (2000)
28. Tarcan, G.; Akıncı, G.; Danişman, M.A.: Assessment of the pollution from tannery effluents upon waters and soils in and Around Kula Vicinity, Turkey. *Water Air Soil Pollut.* **213**, 199–210 (2010). <https://doi.org/10.1007/s11270-010-0378-0>
29. Sözbilir, H.; Baba, A.; Koca, B.; Kiray, H.N.; Karaş, M.: Tectonic setting and hydrogeochemical properties of the geothermal system of Kula Volcanic region, Western Anatolia, Turkey. In: *Proceedings World Geothermal Congress 2020+1 Reykjavik, Iceland* (2021)
30. Schoeller, H.: *Les eaux souterraines. Hydrologie dynamique et chimique, Recherche, Exploitation et Évaluation des Ressources*. Paris, Masson et Cie, 642pp (1962)
31. Leet, D.L.: *Physical Geology*, 6th edn. Prentice-Hall, Englewood Cliffs (1982)
32. Pentecost, A.; Jones, B.; Renaut, R.W.: What is a hot spring? *Can. J. Earth Sci.* **40**, 1443–1446 (2003). <https://doi.org/10.1139/e03-083>
33. Boschetti, T.; Cortecchi, G.; Toscani, L.; Iacumin, P.: Sulfur and oxygen isotope compositions of Upper Triassic sulfates from Northern Apennines (Italy): palaeogeographic and hydrogeochemical implications. *Geol. Acta* **9**, 129–147 (2011). <https://doi.org/10.1344/105.000001690>
34. Awaleh, M.O.; Boschetti, T.; Adaneh, A.E.; Daoud, M.A.; Ahmed, M.M.; Dabar, O.A.; Soubaneh, Y.D.; Kawalieh, A.D.; Kadieh, I.H.: Hydrochemistry and multi-isotope study of the waters from Hanlé-Gaggadé grabens (Republic of Djibouti, East African Rift System): A low-enthalpy geothermal resource from a transboundary aquifer. *Geothermics* **86**, 101805 (2020). <https://doi.org/10.1016/j.geothermics.2020.101805>



35. Kampschulte, A.; Strauss, H.: The sulfur isotopic evolution of Phanerozoic seawater based on the analysis of structurally substituted sulfate in carbonates. *Chem. Geol.* **204**, 255–286 (2004). <https://doi.org/10.1016/j.chemgeo.2003.11.013>
36. Mutlu, H.; Güleç, N.; Hilton, D.R.; Aydın, H.; Halldórsson, S.A.: Spatial variations in gas and stable isotope compositions of thermal fluids around Lake Van: implications for crust-mantle dynamics in eastern Turkey. *Chem. Geol.* **300–301**, 165–176 (2012). <https://doi.org/10.1016/j.chemgeo.2012.01.026>
37. Bouderbala, A.; Gharbi, B.Y.: Hydrogeochemical characterization and groundwater quality assessment in the intensive agricultural zone of the Upper Chelif plain, Algeria. *Environ. Earth Sci.* **76**, 1–17 (2017). <https://doi.org/10.1007/s12665-017-7067-x>
38. Schoeller, H.: Les échanges de bases dans les eaux souterraines; trois exemples es Tunisie. *Bulletin de la Société Géologique de France* **4**, 389–420 (1934)
39. Şahinci, A.: Doğal Suların Jeokimyası. Reform Matbaası, İzmir (1991)
40. Huang, R.; Ding, X.; Lin, C.T.; Zhan, W.; Ling, M.: Effect of saline fluids on chlorine incorporation in serpentine. *Solid Earth Sci.* **3**, 61–66 (2018). <https://doi.org/10.1016/j.sesci.2018.04.001>
41. Ellis, A.J.; Mahon, W.A.J.: Natural hydrothermal systems and experimental hot water/rock interactions (Part II). *Geochim. Cosmochim. Acta* **31**, 519–538 (1967). [https://doi.org/10.1016/0016-7037\(67\)90032-4](https://doi.org/10.1016/0016-7037(67)90032-4)
42. Ellis, A.J.; Mahon, W.A.J.: Natural hydrothermal systems and experimental hot water/rock interactions. *Geochim. Cosmochim. Acta* **28**, 1323–1357 (1964). [https://doi.org/10.1016/0016-7037\(64\)90132-2](https://doi.org/10.1016/0016-7037(64)90132-2)
43. Anselmi, B.; Mellini, M.; Viti, C.: Chlorine in the Elba, Monti Livornesi and Murlo serpentines: evidence for sea-water interaction. *Eur. J. Miner.* **12**, 137–146 (2000). <https://doi.org/10.1127/0935-1221/2000/0012-0137>
44. Rucklidge, J.C.; Patterson, G.C.: The role of chlorine in serpentinization. *Contrib. Miner. Petrol.* **65**, 39–44 (1977). <https://doi.org/10.1007/BF00373568>
45. Rucklidge, J.: Chlorine in partially serpentinized dunite. *Econ. Geol.* **67**, 38–40 (1972). <https://doi.org/10.2113/gsecongeo.67.1.38>
46. Scambelluri, M.; Müntener, O.; Ottolini, L.; Pettke, T.T.; Vanucci, R.: The fate of B, Cl and Li in the subducted oceanic mantle and in the antigorite breakdown fluids. *Earth Planet. Sci. Lett.* **222**, 217–234 (2004). <https://doi.org/10.1016/j.epsl.2004.02.012>
47. Sharp, Z.D.; Barnes, J.D.: Water-soluble chlorides in massive seafloor serpentinites: a source of chloride in subduction zones. *Earth Planet. Sci. Lett.* **226**, 243–254 (2004). <https://doi.org/10.1016/j.epsl.2004.06.016>
48. Huang, R.F.; Sun, W.D.; Zhan, W.H.; Ding, X.; Zhu, J.H.; Liu, J.Q.: Influence of temperature, pressure, and fluid salinity on the distribution of chlorine into serpentine minerals. *J. Asian Earth Sci.* **145**, 101–110 (2017). <https://doi.org/10.1016/j.jseaes.2017.04.022>
49. Tokçaer, M.: Boron isotope ratios and origin of boron in thermal fluids of some geothermal areas in Western Anatolia. *J. Fac. Eng. Archit. Gaz.* **38**, 1361–1373 (2023). <https://doi.org/10.17341/gazimmfd.1092227>
50. Vengosh, A.; Gill, J.; Davisson, M.L.; Hudson, G.B.: A multi-isotope (B, Sr, O, H, and C) and age dating (^3H – ^3He and ^{14}C) study of groundwater from Salinas Valley, California: hydrochemistry, dynamics, and contamination processes. *Water Resour. Res.* **38**, 9-1–9-17 (2002). <https://doi.org/10.1029/2001WR000517>
51. Saxena, V.; Ahmed, S.: Dissolution of fluoride in groundwater: a water-rock interaction study. *Environ. Geol.* **40**, 1084–1087 (2001). <https://doi.org/10.1007/s002540100290>
52. Ayoob, S.; Gupta, A.K.: Fluoride in drinking water: a review on the status and stress effects. *Crit. Rev. Environ. Sci. Technol.* **36**, 433–487 (2006). <https://doi.org/10.1080/10643380600678112>
53. Rieder, M.; Huka, M.; Kučerová, D.; Minařík, L.; Obermajer, J.; Povondra, P.: Chemical composition and physical properties of lithium-iron micas from the Krušné hory Mts. (Erzgebirge). *Contrib. Miner. Petrol.* **27**, 131–158 (1970). <https://doi.org/10.1007/BF00371980>
54. Parkhurst, D.L.; Appelo, C.A.J.: User's guide to PHREEQC (Version 2)—A computer program for speciation, batch-reaction, one-dimensional transport, and inverse geochemical calculations. U.S. Geological Survey Water-Resources Investigations Report, 99–4259, 312 (1999)
55. Johnson, J.W.; Oelkers, E.H.; Helgeson, H.C.: SUPCRT-92: a software package for calculating the standard molal thermodynamic properties of mineral, gases, aqueous species, and reactions from 1 to 5000 bar and 0 to 1000 °C. *Comput. Geosci.* **18**, 899–947 (1992). [https://doi.org/10.1016/0098-3004\(92\)90029-Q](https://doi.org/10.1016/0098-3004(92)90029-Q)
56. Mutlu, H.: Chemical geothermometry and fluid–mineral equilibria for the Ömer-Gecek thermal waters, Afyon area, Turkey. *J. Volcanol. Geotherm. Res.* **80**, 303–321 (1998). [https://doi.org/10.1016/S0377-0273\(97\)00051-6](https://doi.org/10.1016/S0377-0273(97)00051-6)
57. Duchi, V.; Minissale, A.; Vaselli, O.; Ancillotti, M.: Hydrochemistry of the Campania region in southern Italy. *J. Volcanol. Geotherm. Res.* **67**, 313–328 (1995). [https://doi.org/10.1016/0377-0273\(94\)00109-T](https://doi.org/10.1016/0377-0273(94)00109-T)
58. Dilaver, A.T.; Aydın, B.; Özyurt, N.N.; Bayarı, C.S.: Türkiye Yağışlarının İzotop İçerikleri (2012–2016). DSI-TAKK ve MGM-AD, Ankara (2018)
59. Craig, H.: Isotopic variations in meteoric waters. *Science* **133**, 1702–1703 (1961). <https://doi.org/10.1126/science.133.3465.1702>
60. Uemura, R.; Matsui, Y.; Yoshimura, K.; Motoyama, H.; Yoshida, N.: Evidence of deuterium excess in water vapor as an indicator of ocean surface conditions. *J. Geophys. Res.* **113**, D19 (2008). <https://doi.org/10.1029/2008JD010209>
61. Pfahl, S.; Sodemann, H.: What controls deuterium excess in global precipitation? *Clim. Past.* **10**, 771–781 (2014). <https://doi.org/10.5194/cp-10-771-2014>
62. Gat, J.R.; Carmi, I.: Evolution of the isotopic composition of the atmospheric water in the Mediterranean Sea area. *J. Geophys. Res.* **75**, 3039–3048 (1970). <https://doi.org/10.1029/JC075i015p03039>
63. Gökgez, A.; Mutlu, H.; Özkul, M.; Yüksel, A.K.: Multiple fluid-mineral equilibria approach to constrain the evolution of thermal waters in the Hisaralan geothermal field, Simav Graben, western Turkey. *Turk. J. Earth Sci.* **30**, 182–203 (2021). <https://doi.org/10.3906/yer-2007-14>
64. Eastoe, C.J.; Watts, C.J.; Ploughe, M.; Wright, W.E.: Future use of tritium in mapping pre-bomb groundwater volumes. *Ground Water* **50**, 87–93 (2012). <https://doi.org/10.1111/j.1745-6584.2011.00806.x>
65. Clark, I.D.; Fritz, P.: *Environmental Isotopes in Hydrogeology*. Lewis Publishers, New York (1997) <https://doi.org/10.1201/9781482242911>
66. Ercan, T.; Matsuda, J.I.; Nagao, K.; Kita, I.: Noble gas isotopic compositions in gas and water samples from Anatolia. In: Erler, A., Ercan, T., Bingöl, E., Örcen, S. (eds.) *Proceedings of the International Symposium on the Geology of the Black Sea Region*, Ankara, Turkey, pp. 197–206 (1995)
67. Mutlu, H.; Atıcı, G.; Durgut, N.C.; Hilton, D.R.; Akar, M.; Cobankaya, M.: Variations in gas isotope compositions of thermal fluids in central Anatolia, Turkey. EGU General Assembly, Geophysical Research Abstracts, vol. 20, Vienna (2018)
68. Chiodini, G.; Frondini, F.; Cardellini, C.; Parello, F.; Peruzzi, L.: Rate of diffuse carbon dioxide earth degassing estimated from



- carbon balance of regional aquifers: the case of central Apennine, Italy. *J. Geophys. Res. Solid Earth* **105**(B4), 8423–8434 (2000). <https://doi.org/10.1029/1999JB900355>
69. Zöldföldi, J.: 5000 Years marble history in Troia and the Troad. Petroarchaeological Study on the Provenance of White Marbles in West Anatolia. PhD Thesis, Eberhard Karls Universität Tübingen (2011)
 70. Plummer, N.; Prestemon, E.C.; Parkhurst, D.L.: An interactive code (NETPATH) for modeling NET geochemical reactions along a flow PATH, version 2.0, U.S. Geological Survey; USGS Earth Science Information Center, Open-File Reports Section (1994)
 71. Barbieri, M.; Boschetti, T.; Barberio, M.D.; Billi, A.; Franchini, S.; Iacumin, P.; Selmo, E.; Petitta, M.: Tracing deep fluid source contribution to groundwater in an active seismic area (central Italy): a combined geothermometric and isotopic ($\delta^{13}\text{C}$) perspective. *J. Hydrol.* **582**, 124495 (2020). <https://doi.org/10.1016/j.jhydrol.2019.124495>
 72. Izbicki, J.A.; Christensen, A.H.; Newhouse, M.W.; Aiken, G.R.: Inorganic, isotopic, and organic composition of high chloride water from wells in a coastal southern California aquifer. *Appl. Geochem.* **20**, 1496–1517 (2005). <https://doi.org/10.1016/j.apgeochem.2005.04.010>
 73. Krouse, H.R.: Sulphur isotope variations in thermal and mineral waters. In: Cadek, J., Paces, T. (eds.) Proceedings of the International Symposium on Water-Rock Interaction. Prague, Czechoslovakia, pp. 340–347 (1976)
 74. Buschendorf, F.; Nielsen, H.; Puchelt, H.; Ricke, W.: Schwefel-Isotopen-Untersuchungen am Pyrit-Sphalerit-Baryt-Lager Meggen/Lenne (Deutschland) und an verschiedenen Devon-Evaporiten. *Geochim. Cosmochim. Acta* **27**, 501–523 (1963). [https://doi.org/10.1016/0016-7037\(63\)90085-1](https://doi.org/10.1016/0016-7037(63)90085-1)
 75. Claypool, G.E.; Holser, W.T.; Kaplan, I.R.; Sakai, H.; Zak, I.: The age curve of sulfur and oxygen isotopes in marine sulfate and their mutual interpretation. *Chem. Geol.* **28**, 199–260 (1980). [https://doi.org/10.1016/0009-2541\(80\)90047-9](https://doi.org/10.1016/0009-2541(80)90047-9)
 76. Chen, J.-S.; Chu, X.-L.: Sulfur isotope composition of Triassic marine sulfates of South China. *Chem. Geol.* **72**, 155–161 (1988). [https://doi.org/10.1016/0168-9622\(88\)90063-2](https://doi.org/10.1016/0168-9622(88)90063-2)
 77. Yan, H.; Pi, D.; Jiang, S.-Y.; Hao, W.; Cui, H.; Robbins, L.J.; Mänd, K.; Li, L.; Planavsky, N.J.; Konhauser, K.O.: Hydrothermally induced ^{34}S enrichment in pyrite as an alternative explanation of the Late-Devonian sulfur isotope excursion in South China. *Geochim. Cosmochim. Acta* **283**, 1–21 (2020). <https://doi.org/10.1016/j.gca.2020.05.017>
 78. Holser, W.T.: Catastrophic chemical events in earth history of the ocean. *Nature* **267**, 403–408 (1977). <https://doi.org/10.1038/267403a0>
 79. Mizutani, Y.; Rafter, T.A.: Oxygen isotopic composition of sulphates. Part 3. Oxygen isotopic fractionation in the bisulphate ion-water system. *N. Z. J. Sci.* **12**, 54–59 (1969)
 80. Dogramaci, S.S.; Herczeg, A.L.; Schiff, S.L.; Bone, Y.: Controls on $\delta^{34}\text{S}$ and $\delta^{18}\text{O}$ of dissolved sulfate in aquifers of the Murray Basin, Australia and their use as indicators of flow processes. *Appl. Geochem.* **16**, 475–488 (2001). [https://doi.org/10.1016/S0883-2927\(00\)00052-4](https://doi.org/10.1016/S0883-2927(00)00052-4)
 81. Robertson, W.D.; Schiff, S.L.: Fractionation of sulphur isotopes during biogenic sulphate reduction below a sandy forested recharge area in south-central Canada. *J. Hydrol.* **158**, 123–134 (1994). [https://doi.org/10.1016/0022-1694\(94\)90049-3](https://doi.org/10.1016/0022-1694(94)90049-3)
 82. Pierre, C.: Isotopic evidence for the dynamic redox cycle of dissolved sulphur compounds between free and interstitial solutions in marine salt pans. *Chem. Geol.* **53**, 191–196 (1985). [https://doi.org/10.1016/0009-2541\(85\)90068-3](https://doi.org/10.1016/0009-2541(85)90068-3)
 83. Truesdell, A.H.: Geochemical techniques in exploration: Summary of section 3. In: Proceedings of the Second UN Symposium on the Development and Use of Geothermal Resources, San Francisco, CA, USA, pp. 53–79 (1976)
 84. Giggenbach, W.F.: Geothermal solute equilibria. Derivation of Na–K–Ca–Mg geothermometers. *Geochim. Cosmochim. Acta* **52**, 2749–2765 (1988). [https://doi.org/10.1016/0016-7037\(88\)90143-3](https://doi.org/10.1016/0016-7037(88)90143-3)
 85. Giggenbach, W.; Gonfiantini, R.; Jangi, B.L.; Truesdell, A.H.: Isotopic and chemical composition of Parbati valley geothermal discharges, North-West Himalaya, India. *Geothermics* **12**, 199–222 (1983). [https://doi.org/10.1016/0375-6505\(83\)90030-5](https://doi.org/10.1016/0375-6505(83)90030-5)
 86. Kharaka, Y.K.; Mariner, R.H.: Chemical geothermometers and their application to formation waters from sedimentary basins. In: Näser, N.D., McCulloh, T.H. (eds.) Thermal History of Sedimentary Basins. Methods and Case Histories, pp. 99–117 (1989). https://doi.org/10.1007/978-1-4612-3492-0_6
 87. Fouillac, C.; Michard, G.: Sodium/lithium ratio in water applied to geothermometry of geothermal reservoirs. *Geothermics* **10**, 55–70 (1981). [https://doi.org/10.1016/0375-6505\(81\)90025-0](https://doi.org/10.1016/0375-6505(81)90025-0)
 88. Fournier, R.O.; Truesdell, A.H.: An empirical Na–K–Ca geothermometer for natural waters. *Geochim. Cosmochim. Acta* **37**, 1255–1275 (1973). [https://doi.org/10.1016/0016-7037\(73\)90060-4](https://doi.org/10.1016/0016-7037(73)90060-4)
 89. Fournier, R.O.: Chemical geothermometers and mixing models for geothermal systems. *Geothermics* **5**, 41–50 (1977). [https://doi.org/10.1016/0375-6505\(77\)90007-4](https://doi.org/10.1016/0375-6505(77)90007-4)
 90. Lloyd, R.M.: Oxygen isotope behavior in the sulphate water system. *J. Geophys. Res.* **73**, 6099–6110 (1968). <https://doi.org/10.1029/JB073i018p06099>
 91. Giggenbach, E.F.; Corrales, R.: Isotopic and chemical composition of water and steam discharges from volcanic-magmatic-hydrothermal system of the Guanacaste Geothermal Province, Costa Rica. *Appl. Geochem.* **7**, 309–332 (1992). [https://doi.org/10.1016/0883-2927\(92\)90022-U](https://doi.org/10.1016/0883-2927(92)90022-U)
 92. Jeong, C.; Lee, Y.; Lee, Y.; Ahn, S.; Nagao, K.: Geochemical composition, source and geothermometry of thermal water in the Bugok Area, South Korea. *Water* **14**, 3008 (2022). <https://doi.org/10.3390/w14193008>
 93. Giggenbach, W.F.; Goguel, R.L.: Collection and analysis of geothermal and volcanic water and gas discharges. NZ DSIR Chemistry Report 2401, pp. 1–82 (1989)
 94. Das, P.; Maya, K.; Padmalal, D.: Hydrochemistry, geothermometry and origin of the low-temperature thermal springs of South Konkan region, India. *Geothermics* **90**, 101997 (2021). <https://doi.org/10.1016/j.geothermics.2020.101997>
 95. Cortecchi, G.: Oxygen isotopic ratios of sulfate ions-water pairs as a possible geothermometer. *Geothermics* **3**, 60–64 (1974). [https://doi.org/10.1016/0375-6505\(74\)90021-2](https://doi.org/10.1016/0375-6505(74)90021-2)
 96. McKenzie, W.F.; Truesdell, A.H.: Geothermal reservoir temperatures estimated from the oxygen isotope compositions of dissolved sulfate and water from hot springs and shallow drill-holes. *Geothermics* **5**, 51–61 (1977). [https://doi.org/10.1016/0375-6505\(77\)90008-6](https://doi.org/10.1016/0375-6505(77)90008-6)
 97. Nicholson, K.: Geothermal Fluids: Chemistry and Exploration Techniques. Springer, Berlin (1993) <https://doi.org/10.1007/978-3-642-77844-5>
 98. Boschetti, T.: Oxygen isotope equilibrium in sulfate-water systems: a revision of geothermometric applications in low-enthalpy systems. *J. Geochem. Explor.* **124**, 92–100 (2013). <https://doi.org/10.1016/j.gexplo.2012.08.011>
 99. Friedmann, I.; O’Neil, J.R.: Compilation of Stable Isotope Fractionation Factors of Geochemical Interest. USGS Numbered Series (report), 440-KK (1977). <https://doi.org/10.3133/pp440KK>
 100. Kim, S.-T.; O’Neil, J.R.: Equilibrium and nonequilibrium oxygen isotope effects in synthetic carbonates. *Geochim. Cosmochim.*

- Acta **61**, 3461–3475 (1997). [https://doi.org/10.1016/S0016-7037\(97\)00169-5](https://doi.org/10.1016/S0016-7037(97)00169-5)
101. Kele, S.; Breitenbach, S.F.M.; Capezzuoli, E.; Meckler, A.N.; Ziegler, M.; Millan, I.M.; Kluge, T.; Deák, J.; Hanselmann, K.; John, C.M.; Yan, H.; Liu, Z.; Bernasconi, S.M.: Temperature dependence of oxygen and clumped isotope fractionation in carbonates: a study of travertines and tufas in the 6–95 °C temperature range. *Geochim. Cosmochim. Acta* **168**, 172–192 (2015). <https://doi.org/10.1016/j.gca.2015.06.032>
102. Pentecost, A.: *Travertine*. Springer, Berlin (2005)
103. Mutlu, H.; Karabacak, V.; Deniz, K.; Erkkila, B.R.: Multiple geochemical, mineralogical and isotopic approaches to constrain the deposition conditions of Gazlıgöl travertines, western Turkey. *Appl. Geochem.* **139**, article no 105260 (2022). <https://doi.org/10.1016/j.apgeochem.2022.105260>
104. Güleç, N.; Hilton, D.R.; Mutlu, H.: Helium isotope variations in Turkey: relationship to tectonics, volcanism and recent seismic activities. *Chem. Geol.* **187**, 129–142 (2002). [https://doi.org/10.1016/S0009-2541\(02\)00015-3](https://doi.org/10.1016/S0009-2541(02)00015-3)

